

# Identification of Absorption Lines of Heavy Metals in the Wavelength Range 0.97–1.32 $\mu$ m

NORIYUKI MATSUNAGA,<sup>1,2</sup> DAISUKE TANIGUCHI,<sup>1</sup> MINGJIE JIAN,<sup>1</sup> YUJI IKEDA,<sup>3,2</sup> KEI FUKUE,<sup>2</sup> SOHEI KONDO,<sup>4,2</sup>  
SATOSHI HAMANO,<sup>5</sup> HIDEYO KAWAKITA,<sup>2,6</sup> NAOTO KOBAYASHI,<sup>4,7,2</sup> SHOGO OTSUBO,<sup>2</sup> HIROAKI SAMESHIMA,<sup>7</sup>  
KEIICHI TAKENAKA,<sup>6</sup> TAKUJI TSUJIMOTO,<sup>5</sup> AYAKA WATASE,<sup>6</sup> CHIKAKO YASUI,<sup>5,2</sup> AND TOMOHIRO YOSHIKAWA<sup>8</sup>

<sup>1</sup>*Department of Astronomy, School of Science, The University of Tokyo, 7-3-1 Hongo, Bunkyo-ku, Tokyo 113-0033, Japan*

<sup>2</sup>*Laboratory of Infrared High-resolution spectroscopy (LiH), Koyama Astronomical Observatory,*

*Kyoto Sangyo University, Motoyama, Kamigamo, Kita-ku, Kyoto 603-8555, Japan*

<sup>3</sup>*Photocoding, 460-102 Iwakura-Nakamachi, Sakyo-ku, Kyoto 606-0025, Japan*

<sup>4</sup>*Kiso Observatory, Institute of Astronomy, School of Science, The University of Tokyo, 10762-30 Mitake, Kiso-machi, Kiso-gun, Nagano 397-0101, Japan*

<sup>5</sup>*National Astronomical Observatory of Japan, 2-21-1 Osawa, Mitaka, Tokyo 181-8588, Japan*

<sup>6</sup>*Department of Physics, Faculty of Science, Kyoto Sangyo University, Motoyama, Kamigamo, Kita-ku, Kyoto 603-8555, Japan*

<sup>7</sup>*Institute of Astronomy, School of Science, The University of Tokyo, 2-21-1 Osawa, Mitaka, Tokyo 181-0015*

<sup>8</sup>*Edechs, 17203 Iwakura-Minami-Osagi-cho, Sakyo-ku, Kyoto 606-0003, Japan*

(Received October 20, 2019; Revised November 25, 2019; Accepted November 25, 2019)

Submitted to ApJS

## ABSTRACT

Stellar absorption lines of heavy elements can give us various insights into the chemical evolution of the Galaxy and nearby galaxies. Recently developed spectrographs for the near-infrared wavelengths are becoming more and more powerful for producing a large number of high-quality spectra, but identification and characterization of the absorption lines in the infrared range remain to be fulfilled. We searched for lines of the elements heavier than the iron group, i.e., those heavier than Ni, in the *Y* (9760–11100 Å) and *J* (11600–13200 Å) bands. We considered the lines in three catalogs, i.e., Vienna Atomic Line Database (VALD), the compilation by R. Kurucz, and the list published in 1999 by Meléndez & Barbuy. Candidate lines were selected based on synthetic spectra and the confirmation was done by using WINERED spectra of 13 supergiants and giants within FGK spectral types (spanning 4000–7200 K in the effective temperature). We have detected lines of Zn I, Sr II, Y II, Zr I, Ba II, Sm II, Eu II, and Dy II, in the order of atomic number. Although the number of the lines is small, 23 in total, they are potentially useful diagnostic lines of the Galactic chemical evolution, especially in the regions for which interstellar extinction hampers detailed chemical analyses with spectra in shorter wavelengths. We also report the detection of lines whose presence was not predicted by the synthetic spectra created with the above three line lists.

**Keywords:** line: identification — techniques: spectroscopic — stars: abundances — supergiants — infrared: stars

## 1. INTRODUCTION

The identification of stellar absorption lines in the near-infrared range is not complete compared to the established lists of lines in the optical (see, e.g., [Andreasen et al. 2016](#)). In this work, we focus on the el-

ements with the atomic number  $Z \geq 29$ , i.e., those heavier than the iron group elements of which the heaviest is Ni. Those heavy elements are useful for studying the detailed chemical evolution of the Galaxy ([McWilliam 1997](#); [Snedden et al. 2008](#); [Delgado Mena et al. 2017](#)), although their absorption lines are rather limited. The so-called neutron-capture (*n*-capture) elements usually stand for the elements with  $Z \geq 31$  (e.g., [Snedden et al. 2008](#)), and they are mostly synthesized in the presence of excessive neutrons. Depending on the density of

neutrons and the resultant time scale of the  $n$ -capture process, compared with the time scale of the  $\beta$  decay, the  $n$ -capture nucleosynthesis has two main modes,  $s$ -process (slow) and  $r$ -process (rapid), and they occur at different astronomical sites. In contrast, Cu ( $Z = 29$ ) and Zn ( $Z = 30$ ) are often included in the “iron peak” elements and not in the  $n$ -capture elements; the origins of these two elements are, however, considered to be multiplex and complicated (Delgado Mena et al. 2017). We will further discuss, in the Discussion (Section 4.1), the groups of the heavy elements and the insights that can be yielded by the elements with absorption lines confirmed in this study.

We here investigate the absorption lines that appear in near-infrared spectra of FGK-type stars, in particular, supergiants. We have two main reasons for considering supergiants: (i) many absorption lines are expected to be strong in stars with low surface gravity as we see below, and (ii) their high luminosities are advantageous as stellar tracers of the Galaxy and nearby galaxies. In particular, Cepheid variable stars are supergiants within the range of FGK types, aged at 10–300 Myr, and they are useful for studying the Galactic disk because their distances and ages can be accurately estimated (see, e.g., the review by Matsunaga et al. 2018). For example, da Silva et al. (2016) investigated abundances of five  $n$ -capture elements (Y, La, Ce, Nd, and Eu) in hundreds of Cepheids, of which 73 were observed by the authors themselves. They used optical high-resolution spectra for measuring six Y II, six La II, three Ce II, six Nd II, and two Eu II lines which are located between 4500 and 8000 Å (see also Lemasle et al. 2013). In addition, measurements of the heavy elements in Cepheids and supergiants, based on the line list of Kovtyukh & Andrievsky (1999), are found in a series of papers by Luck and collaborators (Luck et al. 2011; Luck & Lambert 2011; Luck 2018, and references therein). The number of the lines used in the previous studies is not so large, and yet they provide us with valuable information on the chemical enrichment of the Galactic disk. Identification and characterization are less advanced for absorption lines in the infrared range, but many efforts have gradually increased the lines available for measuring stellar abundances.

Meléndez & Barbuy (1999; hereinafter referred to as MB99) used the solar spectrum (Kitt Peak Solar Atlas; Wallace et al. 1996, and references therein) to compile the oscillator strengths,  $\log gf$ , and other parameters of the 978 lines that they identified between 10000 and 13400 Å, a part of the  $YJ$  bands, in addition to the 1240 lines in the  $H$  band. We use this MB99 line list as a starting point of our line selection in addition to Vienna

Atomic Line Database (VALD; Ryabchikova et al. 2015) and the compilation by R. Kurucz (KURZ; updated at his web site<sup>1</sup>). The latter two give more general compilations of absorption lines including those purely based on theoretical calculations.

In the recent decade, high-resolution spectrographs covering infrared wavelengths have been used to explore absorption lines including weak ones. For example, dozens of absorption lines of the heavy elements ( $Z \geq 29$ ) have been found (e.g., Hasselquist et al. 2016; Cunha et al. 2017; Afşar et al. 2018; Böcek Topcu et al. 2019; Chojnowski et al. 2019) with high-quality spectra from the APOGEE survey (Majewski et al. 2017) and IGRINS (Park et al. 2014), although they do not cover the  $YJ$  bands of our interest. In contrast, GIANO (Oliva et al. 2012) covers the  $YJ$  bands in addition to  $H$  and  $K$ . Origlia et al. (2013, 2016) measured Sr abundances using one or two lines with GIANO  $Y$ -band spectra. These two studies by Origlia et al. targeted red supergiants in stellar clusters. In contrast, Caffau et al. (2016) investigated GIANO spectra of FG-type dwarfs and found three Sr I lines in the  $Y$  band. Some warmer stars provide us with unique data useful for identifying various absorption lines. Hubrig et al. (2012) reported one Sr II line and one Dy II line in the  $Y$  band in one or more peculiar A-type stars by investigating the spectra from CRIRES (Kaeufl et al. 2004).

The studies mentioned in the preceding paragraph mark important progress in the identification and characterization of absorption lines in the near infrared, but the current list of confirmed lines is clearly incomplete. In this paper, we investigate the lines of the heavy elements with  $Z \geq 29$  seen in the observed spectra, covering the  $YJ$  bands, collected with the near-infrared spectrograph, WINERED.<sup>2</sup> It is a high-resolution echelle spectrograph covering the wavelength range of 0.90–1.35  $\mu\text{m}$  with the resolving power of 28000 or higher (Ikeda et al. 2016; Otsubo et al. 2016). We use WINERED spectra of supergiants and giants with various effective temperatures,  $T_{\text{eff}}$ , between 4000 and 7200 K. The dependency on the temperature varies from line to line, and the set of the WINERED spectra enables us to check whether the absorption at the wavelength of each candidate line depends on  $T_{\text{eff}}$  as expected for the particular line. The purpose of this study is to confirm the absorption lines of the heavy elements that are seen in the  $YJ$ -band spectra of FGK-type stars.

## 2. SPECTRAL DATA

<sup>1</sup> <http://kurucz.harvard.edu/linelists/gfnew/>

<sup>2</sup> <http://merlot.kyoto-su.ac.jp/LIH/WINERED/>

### 2.1. Observational spectra

We investigate  $YJ$ -band spectra of 13 stars, supergiants and giants. Their spectra were obtained in 2015 and 2016 with WINERED attached to the 1.3 m Araki Telescope at Koyama Astronomical Observatory in Kyoto, Japan. The spectral resolution of WINERED with the setting of the WIDE mode and the  $100\mu\text{m}$  slit is around 28000 (Ikeda et al. 2016). We observed dozens of supergiants, giants, and dwarfs whose temperatures were derived making use of the line-depth ratios by Kovtyukh et al. (2003, 2006) and Kovtyukh (2007). The entire set of the spectra for these objects will be considered for discussing the line-depth ratios (Jian et al., in preparation), but a part of the spectra of supergiants and giants are used in this study (Table 1). We use the stellar parameters, including  $T_{\text{eff}}$ , taken from Luck (2014) and Hekker & Meléndez (2007) because they obtained the four necessary parameters, i.e.,  $T_{\text{eff}}$ ,  $\log g$ ,  $[\text{Fe}/\text{H}]$ , and the microturbulence ( $\xi$ ), altogether. Their measurements are based on high-resolution spectra ( $R \geq 40000$ ), and the obtained parameters are precise enough for our purpose; in fact, the spectra synthesized with the given parameters reproduce the observed spectra at around the 1% level as we see below. Figure 1 presents the distribution of the 13 objects on the ( $T_{\text{eff}}$ ,  $\log g$ ) plane.

All the observed spectra were reduced by following the standard procedure adopted in the WINERED pipeline (Hamano et al., in preparation) that was established using PyRAF,<sup>3</sup> which calls IRAF tasks<sup>4</sup> from Python scripts. The reduction steps include sky subtraction, scattered light subtraction, flat-fielding (using a halogen lamp with an integrating sphere), geometric transformation, aperture extraction, and wavelength calibration based on Th–Ar lamp spectra. In addition, small wavelength shifts<sup>5</sup> between individual exposures were corrected, if necessary, before they were combined to give an averaged one-dimensional spectrum for each target. Throughout this paper, we use air wavelengths rather than vacuum wavelengths. Then, the one-dimensional spectrum was normalized at the continuum level, and the telluric correction was performed as described in

<sup>3</sup> PyRAF is a product of the Space Telescope Science Institute, which is operated by AURA for NASA.

<sup>4</sup> IRAF is distributed by the National Optical Astronomy Observatories, which are operated by the Association of Universities for Research in Astronomy, Inc., under cooperative agreement with the National Science Foundation.

<sup>5</sup> The wavelength shifts are, at least partly, due to the instability of the instrument caused by varying ambient temperature, and we made an instrumental upgrade to minimize such shifts in late 2016.

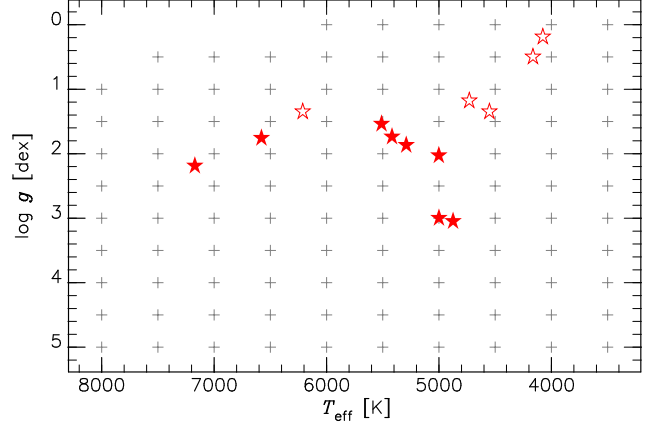


**Figure 1.** Stellar parameters used for spectral synthesis. The effective temperatures,  $T_{\text{eff}}$ , and the surface gravities,  $\log g$ , of our targets (Table 1) are indicated by star symbols, the open symbol for those with  $\log g < 1.5$  and the filled symbol for those with  $\log g > 1.5$ . The gray ‘+’ symbol indicates the grid of ( $T_{\text{eff}}$ ,  $\log g$ ) used for a set of synthetic spectra (Section 2.2).

Sameshima et al. (2018a) using the WINERED spectrum of an A0 V star taken at the same night.

It is worthwhile to add remarks on some objects. Because they are bright, there were studies with optical spectra dating back decades ago, e.g., Steel (1945) for HD 20902 ( $\alpha$  Per). In particular, HD 194093 (or  $\gamma$  Cyg) is an interesting supergiant. Since the early discovery by Adams & Joy (1926, 1927), it is known that the spectrum of  $\gamma$  Cyg is rich in rare-earth lines, e.g., Eu and Dy (see, also, Roach 1942). The star  $\gamma$  Cyg is located close to the so-called  $\gamma$ -Cygni supernova remnant, but Johnson (1975) found that they are not connected with each other.

### 2.2. Synthetic spectra

We used MOOG (the version released in February 2017 Sneden et al. 2012) to create synthetic spectra for selecting and confirming absorption lines of the heavy elements. We adopted the 1D plane-parallel atmosphere models compiled by R. Kurucz.<sup>6</sup> The local thermal equilibrium (LTE) is assumed in the models we used and any part of the spectral synthesis. We considered two sets of stellar parameters. Those for the first set are listed in Table 1 and used for making direct comparisons between the synthetic and observed spectra. We estimated the broadening of individual objects ( $v_b$ , in the full width at half maximum) including the instrumental resolution

<sup>6</sup> We adopted the files named amXX.dat or apXX.dat where XX is to be replaced by two digits indicating the abundances, not the original ones available in Kurucz (1993), from <http://kurucz.harvard.edu/grids/>.

**Table 1.** Observed objects and their parameters

HD	Name	Sp. Type	$T_{\text{eff}}$ (K)	$\log g$ (dex)	[Fe/H] (dex)	$\xi$ ( $\text{km s}^{-1}$ )	Ref.	Obs. Date (UT)	$v_b$ ( $\text{km s}^{-1}$ )	$\gamma$
25291	HR 1242	F0 II	7171	2.19	+0.03	1.67	1	2015.10.28	12.65	1.103
20902	$\alpha$ Per	F5 Ib	6579	1.76	+0.15	3.65	1	2015.10.26	25.61	1.694
194093	$\gamma$ Cyg	F8 Ib	6212	1.35	+0.05	4.02	1	2015.10.26	16.64	1.386
204867	$\beta$ Aqr	G0 Ib	5511	1.54	+0.03	3.39	1	2015.10.26	17.60	1.535
26630	$\mu$ Per	G0 Ib	5418	1.74	+0.09	3.02	1	2015.10.28	17.93	1.362
159181	$\beta$ Dra	G2 Ib–IIa	5291	1.87	+0.15	2.72	1	2016.02.03	18.10	1.198
77912	HR 3612	G7 IIa	5001	2.03	+0.12	2.16	1	2016.03.21	14.27	1.012
27697	$\delta$ Tau	G9.5 III	5000	3.00	+0.08	1.50	2	2015.10.25	12.31	0.957
19787	$\delta$ Ari	G9.5 IIIb	4875	3.05	+0.09	1.68	2	2016.03.11	12.07	0.917
208606	HR 8374	G8 Ib	4731	1.18	+0.25	3.49	1	2015.10.31	17.05	0.896
9900	HR 461	K0 II	4552	1.35	+0.19	2.46	1	2015.10.31	13.51	0.815
206778	$\epsilon$ Peg	K2 Ib–II	4165	0.50	−0.01	2.96	1	2015.10.31	14.73	1.409
52005	HR 2615	K3 Ib	4077	0.19	−0.07	2.76	1	2015.10.28	14.18	1.557

NOTE—Parameters of each target are taken from one of the two references, Ref. 1=[Luck \(2014\)](#) and Ref. 2=[Hekker & Meléndez \(2007\)](#). In the last two columns,  $v_b$  indicates the broadening width including the instrumental profile which corresponds to  $\sim 10.7 \text{ km s}^{-1}$ , and  $\gamma$  indicates the factor we used to convert the depths (see Section 3.2). Spectral types are taken from the SIMBAD database.

based on several isolated lines in the observed spectra. For the second set, we used the  $T_{\text{eff}}$  and  $\log g$  values on the grid indicated by the ‘+’ points in Figure 1 together with the following parameters fixed: the microturbulence  $\xi = 2 \text{ km s}^{-1}$ , the broadening  $v_b = 10.7 \text{ km s}^{-1}$ , and the chemical abundances to be solar ([Asplund et al. 2009](#)). The fixed microturbulence and broadening are not optimal for stars with broad ranges of  $T_{\text{eff}}$  and  $\log g$ . The  $\xi$  of  $2 \text{ km s}^{-1}$  is typical for red giants, but  $\xi$  tends to be larger for stars with higher luminosity ([Gray et al. 2001](#)). The macroturbulence ( $v_{\text{mac}}$ ), or broadening in general, also shows the dependency on the luminosity class ([Gray & Toner 1986](#)). Likewise, both  $\xi$  and  $v_{\text{mac}}$  depend on  $T_{\text{eff}}$  (e.g., [Ryabchikova et al. 2016](#)). This infers that the predicted line strengths in the second set of the synthetic spectra may be biased especially for dwarfs and supergiants. Nevertheless, those synthetic spectra useful to predict where absorption lines in question get significant or deep in the parameter space of ( $T_{\text{eff}}, \log g$ ). Incidentally, the absorption lines we discuss here are mostly shallow and not strongly saturated; therefore,  $\xi$  does not affect our predictions so much.

For both of the sets mentioned above, we assumed the solar abundance ratios of [Asplund et al. \(2009\)](#),  $\log \epsilon_{\text{Fe}, \odot} = 7.50 \text{ dex}$  for  $[\text{Fe}/\text{H}] = 0$  and other ‘Photosphere’ abundances listed in their Table 1, except the carbon abundance. We changed  $[\text{C}/\text{H}]$  by some amounts, between  $-0.31$  and  $0.28 \text{ dex}$ , in order to get

better agreements of CN lines between the synthetic and observed spectra. The observed spectra in the lower temperature range show many CN lines, and those lines are not well reproduced by the synthetic spectra of many stars without the changes. This may be caused by the surface abundance ratios modified by the first dredge-up ([Luck, & Lambert 1985](#); [Takeda et al. 2013](#); [Lyubimkov et al. 2015](#)). The purpose of this adjustment is merely to get the synthetic spectra that match better with the observed ones. The  $[\text{C}/\text{H}]$  values we used are not necessarily accurate estimates of the carbon abundances; therefore, we do not give the  $[\text{C}/\text{H}]$  used for individual objects. In contrast,  $[\text{C}/\text{H}]$  is fixed to be solar in the second set of synthetic spectra for the grid of ( $T_{\text{eff}}, \log g$ ).

In order to assess the absorption of target lines even if they are contaminated by other lines, we consider four kinds of synthetic spectra: (i) normal ones with all lines included, (ii) those with lines of only one species (i.e., each atom or atomic ion) included, (iii) those with only one target line included, and (iv) those with the target lines excluded. We consider the  $\log gf$  values and other parameters of a given target line in each of the three lists. For other atomic lines, we adopted the lines and their parameters in KURZ when we considered target lines in the KURZ list, but we used the VALD line list for considering target lines in VALD or those in MB99. The KURZ list we used is the version compiled

on 2017 Oct 8, while we downloaded the VALD3 list to use on 2019 August 27. For molecular lines, we used those listed in VALD, in which lines of  $C_2$ , CH, CN, CO, and OH molecules are included within the wavelength range of our interest. Only CN lines appear significant in the temperature ranges we investigate. In addition, we adopted FeH lines compiled by Plez (private communication; see also Önehag et al. 2012). We adopted the FeH's dissociation energy of 1.59 eV, at 273.15 K, from Schultz & Armentrout (1991). The FeH lines appear only in a few objects with the lowest temperatures.

In comparing the observed and synthetic spectra of the 13 objects, we noticed dozens of absorption lines which are well visible in the observed spectra but not predicted in the synthetic ones. We list such lines and discuss their characteristics in Appendix B.

### 3. DETECTION OF ABSORPTION LINES

#### 3.1. Line selection

We searched for absorption lines of elements heavier than the iron group elements in the three line lists, KURZ, VALD, and MB99. Combining the three lists, our target elements are from Cu to Th, i.e.,  $29 \leq Z \leq 90$ , with some gaps. We limited ourselves to the ionization states between I (neutral) and III (doubly ionized). We also limited the wavelength ranges to 9760–11100 and 11600–13200 Å, corresponding to the orders of 51–57th ( $Y$  band) and 43–48th ( $J$  band) of WINERED.

In the given wavelength ranges, MB99 lists 19 lines of 6 species in total, i.e., Zn I, Ge I, Sr II, Y II, La II, and Eu II. MB99 covers the wavelengths longer than 10000 Å only. MB99 actually lists 20 lines of our target species between 10000 and 13400 Å, but one of the lines, Ge I 11125.12, falls within the gap of the target in the wavelength range. There is dense and strong telluric absorption around the Ge I line (see, e.g., Fig. 4 in Sameshima et al. 2018a), and we neglected this line. We consider the 19 lines in MB99 in the next selection step.

In contrast to MB99, VALD and KURZ list large numbers of absorption lines for various elements between Cu and Th. Hundreds of lines are listed for some elements, but we cannot expect to see so many lines of these heavy elements in real stellar spectra as we confirm below. Before we compare the observed spectra with the synthetic ones, we limited the number of candidate lines for each species using the synthetic spectra. We considered the spectra for the grid of  $(T_{\text{eff}}, \log g)$  with lines of only one species included at each time (see Section 2.2). We picked up lines that become deeper than 0.02 in depth in at least one of the synthetic spectra at all the grid

points. 67 lines of 9 species in KURZ and 63 lines of 14 species in VALD were found to be candidates.

There are many overlaps between the lines selected with the three line lists, and there are 108 different lines of 14 species in total; 40, 35, and 5 lines are listed only in KURZ, VALD, and MB99, respectively. All of the 5 lines selected from MB99 only are of Ge I. In the following, we consider whether these lines appear significant in the observed spectra or not and, if detected, examine their temperature dependence in comparison with the synthetic spectra.

#### 3.2. Measurements

A significant fraction of the lines we investigate are expected to be blended with other absorption lines even if they exist, and it is difficult to measure the equivalent widths. We therefore consider depths, i.e.,  $d \equiv 1 - f(\lambda_c)$ , where  $f(\lambda_c)$  is the flux at the line center,  $\lambda_c$ , in normalized spectra.

In order to make direct comparisons between the depths in the observed and synthetic spectra, we perform the normalization to adjust the continuum levels of the two kinds of spectra. The reduction performed by the standard pipeline software for WINERED includes the continuum normalization (see, e.g., Section 3.1 in Taniguchi et al. 2018). Although the synthetic spectra we created for individual objects show reasonable agreements between the observed and synthetic spectra, there are noticeable deviations especially within absorption lines. Such deviations can be attributed to inaccurate  $\log gf$  values (Andreasen et al. 2016; Kondo et al. 2019) and maybe to inaccurate abundances assumed. Moreover, narrow flat parts outside apparent absorption lines are found to be lower than the unity in some spectral regions of the synthetic spectra, but the normal continuum procedure applied to the observed spectra adjusts such regions to be around 1. We therefore match the continuum levels of the observed and synthetic spectra around each target line as follows.

First, we searched for velocity offsets to fix small offsets in the wavelength scale, if any, by minimizing the residuals between the observed and synthetic spectra. For each target line at the wavelength of  $\lambda_c$ , the residuals were calculated for spectral parts around the line center. We used the width of  $\pm 300 \text{ km s}^{-1}$  for the objects with  $T_{\text{eff}} < 5200 \text{ K}$  and the width of  $\pm 1000 \text{ km s}^{-1}$  for the others for this wavelength adjustment. The large width for the warmer stars was necessary to accommodate many absorption lines which enable us to estimate the offset precisely. When we compare the observed and synthetic spectra, the synthetic spectra were pixelized to match the pixels of the observed spectra by integrat-



ing the normalized flux within the wavelength range of each pixel of the latter, and  $f_{\text{syn}}$  indicates the counts of thus digitized spectra. We corrected the observed spectra produced by the pipeline for the velocity offsets;  $f_{\text{obs},0}$  indicates the counts of the observed spectra after this correction.

Second, we considered the pixel-by-pixel ratio between each observed spectrum and the corresponding synthetic one,  $r_{\text{org}} \equiv f_{\text{obs},0}/f_{\text{syn}}$ , for adjusting the continuum level of the former to that of the latter. For the normalization around each target line, we used the adjacent parts on both sides of the line, i.e.,  $\lambda_c - \Lambda_2 < \lambda < \lambda_c - \Lambda_1$  and  $\lambda_c + \Lambda_1 < \lambda < \lambda_c + \Lambda_2$ , where  $\Lambda_1$  and  $\Lambda_2$  are the wavelength steps corresponding to the velocity of  $15 \text{ km s}^{-1}$  and  $100 \text{ km s}^{-1}$ , at around  $\lambda_c$ , respectively. The ratio shows deviations from 1 caused by various errors including the offset and slope in the pre-normalized continuum level of  $f_{\text{obs},0}$  and imperfect reproduction of the stellar spectrum in  $f_{\text{syn}}$ . The ratio, as a function of pixel, of the adjacent parts around each target line was fitted as a linear trend,  $a(\lambda - \lambda_c) + b$ , by minimizing

$$\chi^2 = \sum_{\lambda_i} w_f w_\lambda \{r_{\text{org}}(\lambda_i) - a(\lambda_i - \lambda_c) - b\}^2, \quad (1)$$

where the summation is taken over the pixels,  $\lambda_i$ , within the adjacent ranges mentioned above. The pixels within  $\pm 15 \text{ km s}^{-1}$  around the center were not included. We introduced two weight terms,  $w_f$  and  $w_\lambda$ ,

$$w_f = [f_{\text{syn}}(\lambda_i)]^2, \quad (2)$$

$$w_\lambda = \exp\left(-\frac{|\lambda_i - \lambda_c|}{\Lambda_2}\right). \quad (3)$$

The former depends on the count of  $f_{\text{syn}}$ ; the pixels with flux closer to the continuum are more weighted than the pixels within strong absorption. The latter,  $w_\lambda$ , gives higher weights to the pixels closer to the target line in wavelength than to those more separated. Admittedly, we have no solid mathematical background to use the weights as given in Equations (2) and (3). Nevertheless, after some experiments, we found that they tend to give reasonable results even if the observed spectra show deviations from the synthetic one such as lines with clearly different depths. Next, we divided the original observed spectra by the fitted linear trend to obtain the re-normalized spectra,  $f_{\text{obs}}(\lambda) = f_{\text{obs},0}(\lambda)/[a(\lambda - \lambda_c) + b]$ . We also calculated the weighted standard deviation of the residual between the observed and synthetic spectra,

$$e = \sqrt{\frac{\sum \{w_f w_\lambda [f_{\text{obs}}(\lambda_i) - f_{\text{syn}}(\lambda_i)]^2\}}{\sum w_f w_\lambda}}. \quad (4)$$

This  $e$  serves as the error in depth when we compare the depths of the line in the observed and synthetic spectra. The residual is attributed to various factors including pixel-to-pixel errors in the observed spectra, the inconsistency between the observed and synthetic spectra, and the error in the normalization. The median of the  $e$  values calculated for individual ranges around the target lines is  $\sim 0.01$  or smaller for most of the 13 objects. For the two objects with  $T_{\text{eff}} < 4200 \text{ K}$ , however, the median  $e$  values are nearly 0.02. We note that the error estimates described here do not include the uncertainty concerning the target lines themselves because the normalization and the calculations of  $e$  were done without considering the pixels within  $\Lambda_1 = 15 \text{ km s}^{-1}$  around the lines. The residuals at the target wavelengths, if significant, would tell us the inconsistency between the depths observed and those predicted with the line lists.

Then, we measured the depths,  $d$ , at the line wavelength,  $\lambda_c$ , by linearly interpolating the two adjacent pixels,  $\lambda_i$  and  $\lambda_{i+1}$ , with  $\lambda_i \leq \lambda_c < \lambda_{i+1}$ ;  $d_{\text{obs}}$  and  $d_{\text{syn}}$  indicate the depths measured with  $f_{\text{obs}}$  and  $f_{\text{syn}}$ , respectively. While the two depths of each target line can be directly compared with each other for each object, the depths for different objects are affected by differences in various stellar parameters. Here we consider the indicator,  $d^* = \gamma d$ , i.e., the depths multiplied by the factor  $\gamma$  which compensates the effects of stellar metallicity and line width,

$$\gamma \equiv 10^{-[\text{Fe}/\text{H}]} \left( \frac{v_b}{v_{\text{inst}}} \right), \quad (5)$$

where the first term compensates the metallicity effect and the second term converts the depths in spectra broadened by the width of  $v_b$  ( $\simeq \sqrt{v_{\text{mac}}^2 + v_{\text{inst}}^2}$ ) into those in the spectra merely broadened by the instrumental line width,  $v_{\text{inst}} = 10.7 \text{ km s}^{-1}$ , of the WIDE mode of WINERED (i.e., with the broadening by macroturbulence,  $v_{\text{mac}}$ , ignored). The  $\gamma$  factor for each target is listed in Table 1. It should be noted that  $d^*$  does not necessarily agree with the depth of a line in the spectrum of a star with  $[\text{Fe}/\text{H}] = 0 \text{ dex}$  broadened by the instrumental width if the line is blended with other lines. Nevertheless, the conversion from  $d$  to  $d^*$  makes it easier to compare the depths of 13 targets directly and examine the dependence on  $T_{\text{eff}}$ . The  $d^*$  may still be affected by  $\log g$  and  $\xi$ . We will take into account the effect of  $\log g$  by considering the depths in the synthetic spectra obtained for the grid of  $(T_{\text{eff}}, \log g)$  that was described in Section 2.2. On the other hand,  $\xi$  has little impact on shallow lines for which we need precise measurements for confirming the line identification.

Finally, we evaluate the indicator that measures the absorption of the target lines themselves. As mentioned in Section 2.2, we synthesized the spectra with the target lines excluded. Their depths at the wavelengths in question are also measured and denoted as  $d_{\text{syn}\dagger}$ . They are expected to be zero if there is no blending line, but they are often not zero. By subtracting  $d_{\text{syn}\dagger}$  from the normal depth, we can estimate the contribution of a target line to absorption. We calculated this indicator,  $\alpha$ , for the depths in both observed and synthetic spectra;  $\alpha_{\text{obs}} \equiv d_{\text{obs}} - d_{\text{syn}\dagger}$  and  $\alpha_{\text{syn}} \equiv d_{\text{syn}} - d_{\text{syn}\dagger}$ . If  $\alpha_{\text{obs}}$  is large with respect to  $e$ , the absorption by the target line is suggested to be significant. When we compare the measurements for the 13 objects, we consider the conversion by considering the effects of metallicity and broadening,  $\alpha^* \equiv d^* - d_{\text{syn}\dagger}^* = \gamma(d - d_{\text{syn}\dagger})$ , where  $\alpha^*$  and  $d^*$  are considered for both the observed and synthetic spectra. In addition, we use  $\beta \equiv d_{\text{syn}\dagger}/d_{\text{syn}}$  as the estimate of the blend;  $\beta$  varies from 0 (no blend) to 1 (fully contaminated). We define  $\beta = 1$  when  $d_{\text{syn}} = 0$ , but we are not interested in such cases because our purpose is to confirm or reject predicted lines.

### 3.3. Results

We measured the depths,  $d_{\text{obs}}$  and  $d_{\text{syn}}$ , and also the errors,  $e$ , for the 108 candidate lines, selected in Section 3.1, in the spectra of the 13 objects. While many lines were not seen, there are dozens of lines showing large  $\alpha_{\text{obs}}/e$  values. We considered the lines with  $\alpha_{\text{obs}}/e > 2$  to be significant unless they are affected by spurious noises too much. Then, we examined the  $d^*$ ,  $\alpha^*$ , and  $\beta$  plotted against  $T_{\text{eff}}$  (Figure 2) and checked if the dependence on  $T_{\text{eff}}$  is consistent with the expectation from the synthetic spectra. For some lines, the gravity effect on the depths measured for the targets with different  $\log g$  is significant, and we took it into account by comparing the  $T_{\text{eff}}$  trends expected for the two  $\log g$  values, 0.5 and 2.5, illustrated in Figure 2. In addition, we checked the appearance of the spectra, comparing the synthetic spectra with the target lines removed with the observed spectra (see Figure 3), as well as how the telluric absorption could have left noises after the correction.

Among the 108 lines we examined in the observed spectra (Section 3.1), we detected 23 lines (Table 2). Figure 3 presents the spectra of some stars with the line detected. We here summarize the characteristics of the lines we identified, but more details on the lines of individual species are given in Appendix A. We detected two Zn I, three Sr II, and five Y II lines listed in all the three lists, KURZ, VALD, and MB99, but no other lines of these species were confirmed. We also

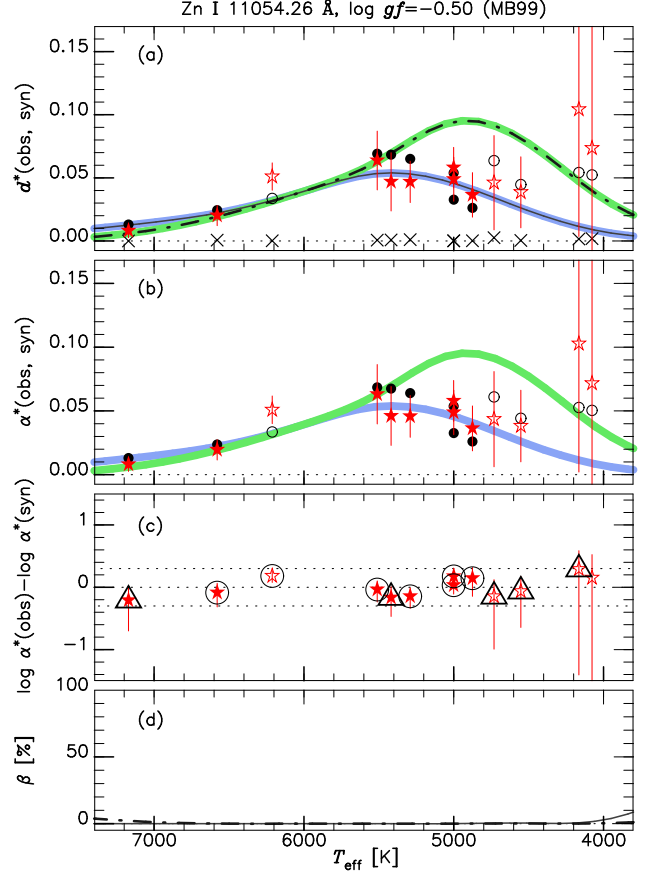


**Figure 2.** The temperature dependency of the line depths and blends. The species and wavelength of the line together with the  $\log gf$  and its source (KURZ, VALD, or MB99) are labeled at the top. The top two panels plot the depths,  $d^*$ , and the contribution of the target lines themselves,  $\alpha^*$ , against  $T_{\text{eff}}$ . Both  $d^*$  and  $\alpha^*$  are after the correction of metallicity and broadening (see Section 3.2). Star symbols indicate the measurements with the observed spectra of 13 objects; the open symbol for those with  $\log g < 1.5$  and the filled symbol for those with  $\log g > 1.5$ . Open and filled circles indicate the values obtained with the synthetic spectra for the objects with  $\log g < 1.5$  (open) and those with  $\log g > 1.5$  (filled). The 'x' symbol in the top panel indicates the depths in the synthetic spectra with the target lines excluded. The green and blue curves in the panels (a) and (b) indicate the  $T_{\text{eff}}$  trend of the target line itself expected for stars with 0.5 and 2.5, respectively, in  $\log g$ , while the dot-dashed and solid curves in the panel (a) indicate the corresponding trends of the depth including blends. In the third panel, we plot  $\log \alpha_{\text{obs}}^* - \log \alpha_{\text{syn}}^* \simeq 0$  and the error against  $T_{\text{eff}}$  for the 13 objects. The star symbols in the panel (c) are accompanied by circles or triangles if we found significant ( $\alpha_{\text{obs}}/e > 2$ ) or marginal ( $1 < \alpha_{\text{obs}}/e < 2$ ) detection. The last panel shows the blends,  $\beta$ , for the synthetic spectra of stars with  $\log g = 0.5$  (dot-dashed) and 2.5 (solid). The complete figure set (23 images) is available in the online journal.

detected one MB99 line of Eu II (10019.52 Å) together

with Eu II 9898.27 and 10165.56 that are not included in MB99. In addition, among the candidate lines which are not in MB99, we identified four Zr I, one Ba II, two Ce II, two Sm II, and one Dy II lines.

A few lines have been already reported in previous papers, besides MB99, based on high-resolution spectra. Although the temperature of the object is different from ours, Sameshima et al. (2018b) identified the two Sr II lines at 10327.31 and 10914.89 Å in a WINERED spectrum of an A0 V-type star. The same lines were used for measuring abundances of red supergiants by Origlia et al. (2013), and the one at 10914.89 Å was also identified by Hubrig et al. (2012) in peculiar A-type stars. In addition to these Sr II lines, we also confirmed the one at 10036.65 Å (a strong line listed in MB99). The Dy II line at 10835.94 Å reported by Hubrig et al. (2012) with spectra of peculiar A-type stars was not confirmed in any of our targets.

The 85 lines We could not confirm 85 candidate lines in the observed spectra. They include some lines listed in MB99: Zn I 13196.62, La II 11874.19, and six Ge I lines (see the notes on the individual elements in the Appendix). We found that there may be absorption by some of the unconfirmed lines, but rejected them either because the lines are not deep enough to be confirmed ( $\alpha_{\text{obs}}/e < 2$ ; e.g., Ce II 9774.63) or the telluric absorption seems to leave spurious noises (e.g., Sm II 9788.96). In addition, we found quite strong absorption at the wavelength of Dy II 10305.36, but did not conclude that the line was confirmed because the observed  $T_{\text{eff}}$  trend is not consistent with the prediction. The Dy II line, if exists, is at least contaminated by an unidentified line.

We examined  $\log \alpha_{\text{obs}}^* - \log \alpha_{\text{syn}}^*$  and judged if the  $\log gf$  values given in the line lists reproduce the depths of significant lines ( $\log \alpha_{\text{obs}}^* - \log \alpha_{\text{syn}}^* \simeq 0$ ) or not. The superscript *c* in Table 2 indicates that the measured depths differ from those predicted with the given  $\log gf$  by  $\sim 0.3$  dex or more. We note, however, that our conclusions on the  $\log gf$  cannot be final because we only made comparisons with the synthetic spectra created with the solar [X/Fe] values assumed.

## 4. DISCUSSION

### 4.1. Astronomical implications

In the following, we discuss the implications that individual elements with the detected line(s) may give to the chemical evolution of the Galaxy and nearby galaxies. We here focus on the chemical imprints one would find in Galactic-disk stars of around the solar metallicity. For stars with different metallicities or those in different systems, some elements may be explained by different origins. For example, Ba is an *s*-process ele-

**Table 2.** Absorption lines identified in the observed spectra

Species	$\lambda_{\text{air}}$ (Å)	EP (eV)	$\log gf$ (dex)		
			KURZ	VALD	MB99
Zn I	11054.26	5.796	−0.20	−0.30	−0.50
Zn I	13053.60 <sup>a</sup>	6.655	+0.39	+0.34	+0.13
Sr II	10036.65	1.805	−1.22	−1.31	−1.10
Sr II	10327.31	1.839	−0.25	−0.35	−0.40
Sr II	10914.89	1.805	−0.57	−0.64	−0.59
Y II	10105.52	1.721	−1.63	−1.89	−1.89
Y II	10186.46	1.839	−2.65 <sup>c</sup>	−2.65 <sup>c</sup>	−1.97
Y II	10245.22	1.738	−1.82	−1.82	−1.91
Y II	10329.70	1.748	−1.51	−1.76	−1.71
Y II	10605.15	1.738	−1.71	−1.96	−1.89
Zr I	9822.56	0.623	−1.44	−1.20	—
Zr I	10654.18	1.582	−1.32	—	—
Zr I	11612.67	1.366	−0.88	—	—
Zr I	11658.07	1.396	−0.56	—	—
Ba II	13057.72 <sup>b</sup>	5.251	+0.34 <sup>c</sup>	+0.34 <sup>c</sup>	—
Ce II	9805.49	0.322	—	−3.23 <sup>c</sup>	—
Ce II	9853.11	0.704	—	−2.49 <sup>c</sup>	—
Sm II	9850.67	1.971	—	−0.46 <sup>c</sup>	—
Sm II	9936.51	1.890	—	−0.61	—
Eu II	9898.30	2.108	−0.76 <sup>c</sup>	−0.07	—
Eu II	10019.52	2.091	−0.66 <sup>c</sup>	−0.66 <sup>c</sup>	−0.30
Eu II	10165.56	2.108	−0.78	−0.78	—
Dy II	10523.39	1.946	—	−0.45	—

<sup>a</sup>The wavelength in the KURZ list, 13053.559 Å, is slightly different from the counterparts in the VALD, 13053.627 Å, and the MB99, 13053.64 Å.

<sup>b</sup>The wavelength in the KURZ list, 13057.716 Å, is shorter than the counterpart in the VALD, 13058.015 Å.

<sup>c</sup> The measured depths differ from those predicted with the given  $\log gf$  by  $\sim 0.3$  dex or more.

ment at around the solar metallicity but the contribution of the *r*-process gets stronger at the low-metallicity range (Burris et al. 2000). Moreover, there are proposed *n*-capture processes that show patterns different from those of the main *s*- and *r*-processes (e.g., Burris et al. 2009; Hampel et al. 2016). Our main targets, supergiants, are young and expected to be relatively metal rich, and previous explanations on the origins of the heavy elements in the Sun and the Solar system (Burris et al. 2000; Sneden et al. 2008) gives at least an approximate idea on the origins of individual elements in the supergiants.



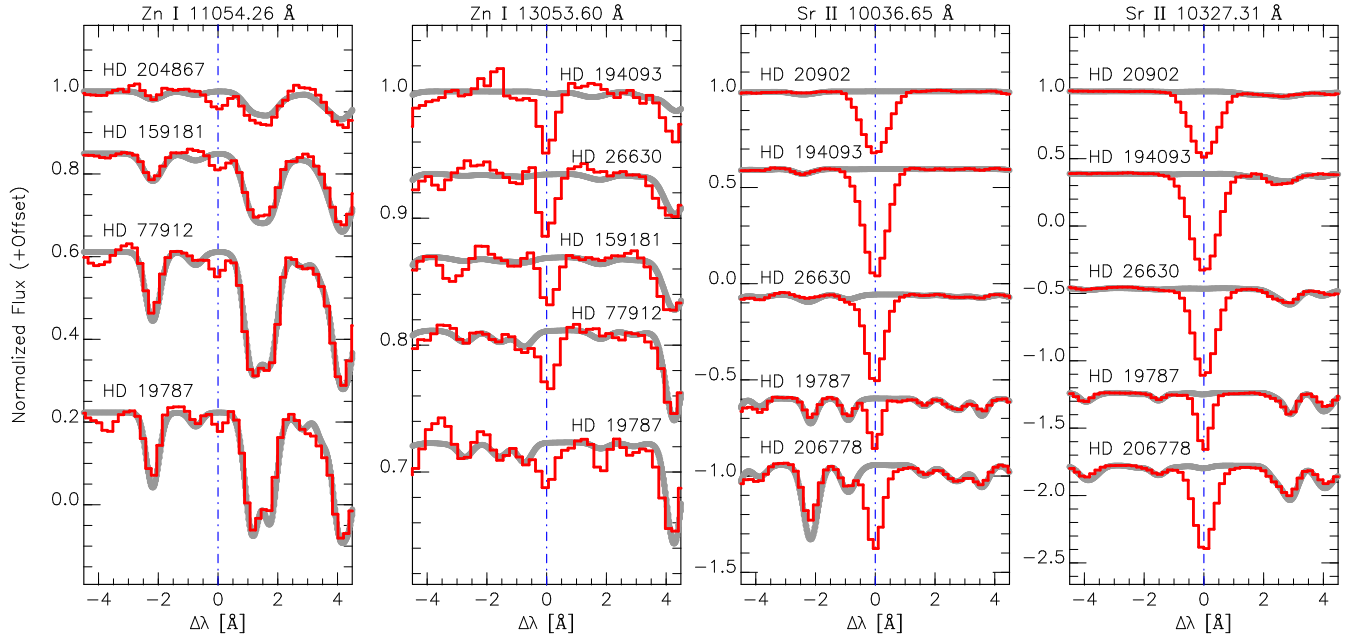


**Figure 3.** Spectra around the absorption lines detected. The species and the air wavelength, indicated by the vertical line, of each line are labeled at the top of each panel. The red and gray curves respectively indicate the observed spectra and the spectra synthesized without the target line included. The complete figure set (23 panels) is available in the online journal.

Zn is often included in the iron peak elements and considered as the heaviest one of this group. In fact, in a broad range of the metallicity down to  $[\text{Fe}/\text{H}] \simeq -2$  dex, Zn in stars in the solar neighborhood shows a concentration around  $[\text{Zn}/\text{Fe}] = 0$  and thus seems to be created along with Fe and other iron peak elements (Snedden et al. 1991). However, it has become clear that systematic differences in the  $[\text{Zn}/\text{Fe}]$  trends are found in different systems (thin and thick disks, bulge, halo, and dwarf galaxies) thanks to the efforts of various authors (Duffau et al. 2017; Ji & Frebel 2018; Hirai et al. 2018, and references therein). The origins of Zn remain still elusive and its implication to the Galactic chemical evolution may be unique compared with other better-understood elements (see, e.g., Tsujimoto & Nishimura 2018).

The  $s$ -process elements are created mainly in low- and intermediate-mass Asymptotic Giant Branch (AGB) stars. Good reviews on the process are found, e.g., in Busso et al. (1999) and Karakas & Lattanzio (2014). Sr, Y, and Zr are grouped as light  $s$ -process elements, although they show slightly different trends from each other in disk stars (Delgado Mena et al. 2017). Ba and Ce are often called heavy  $s$ -process elements together with Nd. The abundance trends of the three heavy  $s$ -process elements are, however, not necessarily common. For example, Andrievsky et al. (2013, 2014) reported that the radial gradient of Ba has a negligible slope, while Lemasle et al. (2013) and da Silva et al. (2016) found significant slopes of the gradient for the other

heavy  $s$ -process elements, Ce and Nd, as well as for Y and Zr, i.e., light  $s$ -process elements. As noted by Andrievsky et al. (2014) and Luck (2014), only strong Ba lines were used with non-LTE calculations, which may leave significant uncertainties. Readers are referred to other studies such as D’Orazi et al. (2009), Bensby et al. (2014), and references therein concerning the Ba abundances by using the strong lines in the optical, but their targets are dwarfs and giants. Ba II 13058.01 found in this study is, in contrast, expected to be weak; therefore, this line may add an important constraint on the Ba abundances. On the other hand, the three Sr II lines in the  $Y$  band are very strong and the same problem of the non-LTE effect may prevent us from obtaining accurate Sr abundances.

Eu is representative of  $r$ -process elements. Sm and Dy are considered to be mainly formed through the  $r$ -process around the solar metallicity (Burris et al. 2000). The contribution of the  $s$ -process to Sm can be larger, especially for some isotopes, but the trend of Sm seen in the disk stars with about the solar metallicity is similar to that of Eu (Battistini & Bensby 2016). After the discovery of the gravitational wave and the electromagnetic counterpart of GW 170817 (Abbott et al. 2017), it has become more evident that the neutron star mergers accompanied by kilonovae are major contributors to  $r$ -process elements (Smartt et al. 2017; Tanaka et al. 2017). However, explaining the chemical evolution of  $r$ -process abundances seen in disk stars requires further investigations concerning some complications due, e.g.,

to the delay-time distributions of the neutron star mergers (Hotokezaka et al. 2018), the initial mass functions (Tsujiimoto, & Baba 2019), and potential contribution from other origins (Siegel et al. 2019). New observational constraints on the  $r$ -process enrichment can be expected if the near-infrared diagnostic lines of Eu and Dy are used for measuring the abundances of stars in unexplored regions of the Galactic disk behind severe interstellar extinction.

#### 4.2. Expected targets

The lines we report here will be useful diagnostic lines of detailed chemical abundances available in the  $YJ$  bands. In order to give a rough idea on the  $(T_{\text{eff}}, \log g)$  range in which the detected lines are seen, we present in Figure 4 the contours of  $\alpha_{\text{syn}} = d_{\text{syn}} - d_{\text{syn}\dagger}$  based on the synthetic spectra obtained for the  $(T_{\text{eff}}, \log g)$  grid (see Figure 1). Some lines are blended and may be difficult to measure the abundances even if  $\alpha$  gets significant. Also, note that the depths refer to those expected for the spectra with the WINERED resolution,  $R = 28000$ , for stars with the solar metallicity,  $[\text{Fe}/\text{H}] = 0$  dex, and sufficiently small broadening. Nevertheless, the contours will be useful, e.g., for selecting the targets to study the abundances discussed in this paper and making the observational plans to achieve the detection of the lines.

Only two species (Zn I and Zr I) among the 9 with the lines detected are neutral. In contrast, the others are singly ionized. The first ionization potentials of the elements with the detected lines are low, 5.2–6.2 eV, compared to Zn (9.4 eV) and Zr (6.6 eV). The lines of the ionized species are sensitive to  $\log g$  and strong in low-gravity stars as expected. Furthermore, Figure 4 indicates that supergiants with  $T_{\text{eff}} \sim 5000$  K and  $\log g \lesssim 1.5$  dex show the strongest absorption of the lines of Sr II, Y II, Ba II, Sm II, Eu II, and Dy II. The contours of Zn I are similar to those of the above species to some extent, the peak being around 5000 K and stronger towards the lower surface gravity, but the sensitivity to the gravity is not so high as the ionized species. In contrast, the lines of Ce II require both low temperature,  $T_{\text{eff}} < 4000$  K, and low surface gravity,  $\log g < 1$ , to be significant. In the case of Zr I, the line strengths grow rapidly towards low  $T_{\text{eff}}$  but are insensitive to surface gravity.

Cepheids have intermediate temperatures, 4500–6500 K, and low surface gravities,  $\log g \lesssim 1.5$  dex (see, e.g., Genovali et al. 2014). Their locations on the Hertzsprung-Russell diagram (HRD) thus agree with the peaks of the strengths for most of the lines reported in this paper, although Zr I may be seen only in Cepheids with the lowest  $T_{\text{eff}}$  among this group of pul-

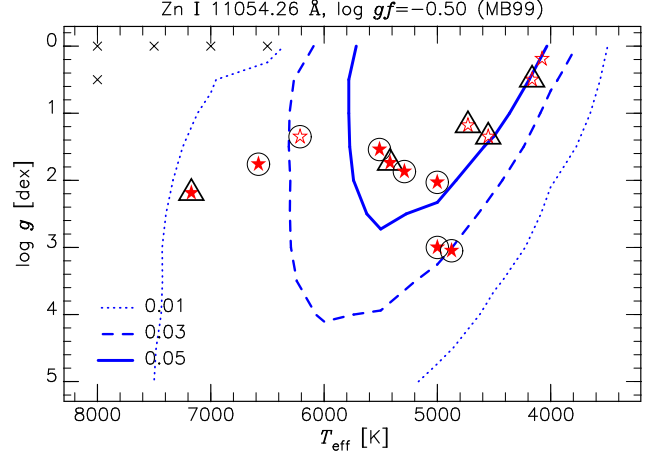


**Figure 4.** Contours of the predicted depths of the lines we detected. The species and wavelength of the line together with the  $\log gf$  and its source (KURZ, VALD, or MB99) are labeled in the top of each panel. The contours of  $\alpha_{\text{syn}}$  for the levels indicated within each panel are created based on the synthetic spectra with the solar abundance and the broadening  $v_b = 10.7 \text{ km s}^{-1}$  for the grid of  $(T_{\text{eff}}, \log g)$  illustrated in Figure 1. We note that the grid lacks the points indicated by the ‘x’ symbol. The star symbols (open if  $\log g < 1.5$  and filled if  $\log g > 1.5$ ) indicate the observed targets in this study, and they are accompanied by circles or triangles if we found significant ( $\alpha_{\text{obs}}/e > 2$ ) or marginal ( $1 < \alpha_{\text{obs}}/e < 2$ ) detection of the line. The complete figure set (23 images) is available in the online journal.

sating stars in the Cepheid instability strip. Therefore,  $YJ$ -band spectra of Cepheids would allow us to measure various heavy elements including both  $s$ - and  $r$ -process elements and also those with mixed origins such as Zn.

Cepheids are young, 10–300 Myr old, and provide valuable information on chemical abundances of the present Galaxy. It is known that their metallicities are anti-correlated with the distances from the Galactic center ( $R_{\text{GC}}$ ), known as the abundance gradient (Genovali et al. 2014). Observing Cepheids in a wide range of  $R_{\text{GC}}$  thus allows investigating the abundance patterns from the metal-rich end ( $[\text{Fe}/\text{H}] \sim +0.2$  at  $R_{\text{GC}} \leq 6 \text{ kpc}$ ) to the metal-poor end ( $[\text{Fe}/\text{H}] \lesssim -0.3$  at  $R_{\text{GC}} \geq 14 \text{ kpc}$ ) of the current Galactic disk. The youth of Cepheids offers a crucial advantage in studying the disk chemical evolution. The radial migration of the disk (Sellwood & Binney 2002) affects the current abundance distribution of various elements for stars in the disk (e.g., see a recent study on the  $r$ -process abundance in the solar neighborhood by Tsujiimoto, & Baba 2019). Cepheids are, however, considered to be located almost at their birth positions in terms of  $R_{\text{GC}}$  and tell us, at least approximately, the current abundances of star-forming gas. Recent large-scale surveys have

found a large number of new Cepheids spread in a large range of  $R_{GC}$  (Udalski et al. 2018; Chen et al. 2019; Dékány et al. 2019; Skowron et al. 2019), and some of them are heavily reddened in the Galactic disk. Near-infrared spectroscopic observations are desired to obtain their abundances.

Bright red giants, roughly  $T_{\text{eff}} \lesssim 5000$  K and  $1 \lesssim \log g \lesssim 2$  dex, are often targeted for investigating the heavy elements in nearby dwarf galaxies (e.g., McWilliam et al. 2013; Ji et al. 2016; Ji & Frebel 2018). Sr II and Zr I lines are expected to be strong, while Y II lines are probably weak,  $\lesssim 0.05$  in depth. Some Eu II lines may also be seen but the abundance measurements would require high signal-to-noise ratios with the typical depths expected to be around  $\sim 0.02$  or smaller. Observing the lines of other heavy elements would be even more challenging. Bright red giants are important because they are usually the easiest targets in stellar systems like the Galactic bulge and dwarf galaxies which are dominated by old stars. Measuring their Eu abundances, if possible, would be very useful for studying the chemical evolution of those systems together with the  $s$ -process abundances traced with Sr and Zr.

At the lower parts of the Hertzsprung-Russell diagram,  $\log g \lesssim 3$ , only a small fraction of the lines reported in this study are expected to be visible. The three Sr II lines are expected to be still strong,  $\gtrsim 0.2$ , for a wide range of  $T_{\text{eff}}$ . In fact, Caffau et al. (2016) detected the three lines and estimated the abundances by taking into account the non-LTE effect. The two Zn I lines may be seen in stars with intermediate temperatures around 5500 K, while Zr I 9822.56 is expected to be visible only in late-type stars with  $T_{\text{eff}} < 5000$  K. None of the other species is probably significant unless the abundances are highly enhanced.

## 5. SUMMARY

We identified 23 lines of 9 elements heavier than the iron group elements, i.e., Zn, Sr, Y, Zr, Ba, Ce, Sm, Eu, and Dy, using the  $YJ$ -band WINERED spectra of 13 supergiants and giants. Besides the lines we detected, significantly more lines of the targeted heavy elements were selected based on KURZ and/or VALD but not detected. We also found lines that are clearly present in

the observed spectra but are not predicted in the synthetic counterparts (Appendix B). It is vital to establish the list of lines of various elements in the infrared range.

Although we have identified the absorption lines of rare heavy elements, including newly detected lines, there remains a lot to be done. Further searches for new lines should be performed. Our search was done by using WINERED spectra with the resolution of 28000 with the typical S/N around 200–300. It would be useful to make a more complete survey of the relevant absorption lines by using spectra with higher resolution and/or higher quality, although the resolution of 28000 is high enough to resolve the intrinsic line profiles of many supergiants. Solid estimates of  $\log gf$  values are also important for abundance measurements with these lines especially because the numbers of lines are small. For this purpose, our targets and dataset are not optimal. For example, relatively metal-poor stars with enhanced abundances of  $s$ -process or  $r$ -process elements (e.g., Sneden et al. 2008; Bisterzo et al. 2011) would be good calibrators because the lines of the enhanced elements can be measured with reduced line contamination.

We thank Andy McWilliam for useful comments on the analysis and the manuscript. We are grateful to the staff of the Koyama Astronomical Observatory for their support during our observation. This study is financially supported by JSPS KAKENHI (grant No. 16684001, 20340042, 21840052, 26287028, and 18H01248) and the MEXT Supported Program for the Strategic Research Foundation at Private Universities, 2008–2012 (No. S0801061) and 2014–2018 (No. S1411028). HS acknowledges the JSPS grant No. 19K03917. This study has made use of the SIMBAD database, operated at CDS, Strasbourg, France, and also the VALD database, operated at Uppsala University, the Institute of Astronomy RAS in Moscow, and the University of Vienna. We thank the referee, Prof. Robert Kurucz, for comments that helped us to improve this paper.

*Software:* WINERED pipeline (Hamano et al., in preparation), IRAF (Tody 1986, 1993), PyRAF (Science Software Branch at STScI 2012), MOOG (February 2017 version; Sneden et al. 2012).

## APPENDIX

### A. IDENTIFICATION OF LINES OF INDIVIDUAL ELEMENTS

Here we describe the identification (or the failure of confirmation) of the lines of the heavy elements using the WINERED spectra of 13 objects (Table 1). We examined 108 lines of 14 species in total. Table 2 lists the 23 detected lines.

- Zn (Zinc,  $Z = 30$ ) — We investigated four Zn I lines using the observed spectra. The line at 13150.5 Å (13150.464 Å in KURZ and 13150.533 Å in VALD) is not included in MB99, but the other three are included. We clearly detected two lines at 11054.26 and 13053.60 Å, which are free from blends at most of the  $T_{\text{eff}}$  range we investigated. For each line of them, the  $\log gf$  values in KURZ and VALD are consistent within 0.1 dex, but the  $\log gf$  in MB99 is different by 0.15–0.3 dex. The  $\log gf$  values in MB99 seem to give better agreements between the predicted and measured depths for both of the lines although the differences between the three lists are not large. Among the two lines that were not confirmed, Zn I 13150.5 is dominated by the strong blending line, Al I 13150.75. The other one, Zn I 13196.6, also suffers from significant blends especially at lower  $T_{\text{eff}}$ , if exists, and it tends to be affected by telluric lines too. KURZ and VALD list slightly different wavelengths, within 0.1 Å, for the two undetected lines but these lines are not detected in the observed spectra in any case.
- Ga (Gallium,  $Z = 31$ ) — We investigated two Ga I lines, included in both KURZ and VALD, using the observed spectra. Neither of them is included in MB99 although their wavelengths are longer than 10000 Å. They were predicted to be significant,  $\gtrsim 0.02$ , only at the lowest temperatures,  $T_{\text{eff}} \lesssim 4000$  K. Moreover, both of them are strongly blended with other lines ( $\gtrsim 80\%$ ), and we could confirm none of the Ga I lines. Around the wavelength of Ga I 11949.23, Ti I 11949.55 gives strong absorption at lower  $T_{\text{eff}}$  and Ca II 11949.74 gives strong absorption at higher  $T_{\text{eff}}$ . Around Ga I 12109.85, Si I 12110.66 gets stronger towards the lower  $T_{\text{eff}}$ .
- Ge (Germanium,  $Z = 32$ ) — We investigated eight Ge I lines using the observed spectra. All of them are located at longer than 10000 Å. One line at 11714.75 Å is listed in all the three lists. In addition, three lines are listed only in KURZ and VALD, while four lines only in MB99. The Ge I lines are expected to get strongest at around 4500 K, but most of the lines we investigated do not reach 0.05 in  $\alpha_{\text{syn}}^*$  according to the  $\log gf$  values available in the lists. Some lines are expected to be strongly blended while others are not, but we could not confirm any of the Ge I lines. The  $\alpha_{\text{obs}}^*$  we obtained are consistent with zero for almost all of the objects expected to show the Ga absorption, which indicates that the  $\log gf$  values are at least smaller than expected.
- Sr (Strontium,  $Z = 38$ ) — We investigated nine Sr II lines using the observed spectra. Three of them (10036.65, 10327.31, and 10914.89 Å) are listed in all the three line lists. These lines are strong and there are almost no blends. The  $\log gf$  values in the three lists are more-or-less consistent with each other, within 0.2 dex, and they give reasonable agreements between the observed and synthetic spectra. We note that these three lines are very deep and the departures from the predicted depths may well be caused by the factors, other than inaccurate  $\log gf$  values, that were not taken into account in our simple spectral synthesis (e.g., the non-LTE effect). In contrast, we could confirm no other Sr II lines. The reduced spectra of a couple of objects present a hint of Sr II 12974.38, but telluric absorption lines around this wavelength seem to give spurious noise on the spectra. We also found non-zero  $\alpha_{\text{obs}}/e$  for Sr II 12013.96 in a few objects, but the dependency of the depth on  $T_{\text{eff}}$  and  $\log g$  is not consistent with predicted for this line. There is one Fe I line at 12013.88 Å, and the  $\alpha_{\text{obs}}$  we measured could be explained by the error in oscillator strength of this line with a  $\log gf$  larger than listed. For Sr II 13121.96, two entries with different  $\log gf$  values, 0.692 and  $-0.609$  dex, are listed in VALD with the same wavelength and the same excitation potential (EP). Including or excluding the shallower one with  $\log gf = -0.609$  does not change the synthetic spectra significantly and, in any case, the absorption was not confirmed in the observed spectra.
- Y (Yttrium,  $Z = 39$ ) — We investigated two Y I and five Y II lines using the observed spectra. The Y I lines are not included in MB99, while it lists all the Y II lines. The Y I lines were predicted to be visible at very low temperatures, around 3500 K, but still shallow,  $\sim 0.03$ ; we could not confirm them in the observed spectra. In contrast, we detected all the five Y II lines. All of them except Y II 10605.15 are significantly blended at least at  $T_{\text{eff}} \lesssim 5000$  K, but the Y II lines are expected to get deepest at 5000–5500 K and this dependency on  $T_{\text{eff}}$  can be well traced with our measurements. The  $\log gf$  values in MB99 reproduce the observed depths better for Y II 10186.46, while the  $\log gf$  values in the three lists are at least roughly consistent with each other and they predict reasonable depths for the other four lines.
- Zr (Zirconium,  $Z = 40$ ) — We investigated 40 Zr I lines using the observed spectra. Two lines are listed in both KURZ and VALD, while the other 38 lines are found in KURZ only. None of them is listed in MB99. We confirmed four lines in a few objects at low  $T_{\text{eff}}$  without significant blends. One of them is listed in both KURZ and VALD, while the others are given in KURZ only. The  $\log gf$  values in the KURZ list give reasonable

predictions of the depths observed where the detection is significant. We note that the observed and synthetic spectra show poor agreements around Zr I 10654.18 (see the online material for Figure 3). The absorption line observed at around 10657.4 Å is listed as an unknown one in Table 3. In addition, the observed spectra show broad and stronger absorption than the synthetic ones at around 10652 Å, which indicates that more than one lines contribute to the observed absorption but the line lists used for the synthetic spectra give too low  $\log gf$  values or completely miss necessary lines. A part of the inconsistency can be explained by the low  $\log gf$  values, approximately  $-2.8$  dex, of Fe I 10652.24 (EP=5.478 eV) in KURZ and VALD, whose  $\log gf$  in MB99 is significantly higher,  $-1.79$  dex. At least one other line is necessary to explain the wide absorption observed, and CN 10651.796 but with  $\log gf$  higher than given in VALD would probably explain the absorption in combination with the Fe I line.

- Ba (Barium,  $Z = 56$ ) — We investigated one Ba II line using the observed spectra. This line is listed in KURZ and VALD but not in MB99. The wavelengths in the former two catalogs are slightly different, 13057.716 Å in KURZ and 13058.015 Å in VALD. Synthetic spectra indicate: (i) The line gets deepest at around 5300 K. (ii) It becomes shallower and shallower with increasing  $\log g$ , and the  $d^*$  never reaches 0.01 at  $\log g \gtrsim 2.5$  dex. (iii) There are strong blends throughout the temperature range from 4000 to 8000 K; 30 % or higher (reaching almost 100 %) at  $\lesssim 4,500$  K and  $\log g = 0.5$  dex, and 50 % or higher at  $\log g = 2.5$  dex. The absorption by this Ba II line is supported by the observed spectra of a few objects with  $T_{\text{eff}} > 5000$  K where the blends are moderate. The overall result indicates that the detection of this line is solid, but the confirmation based on more spectra is desirable. The observed depths, where significant, are larger than predicted based on the synthetic spectra by a factor of  $\sim 3$ , although this may be because we assumed the solar abundance ratio of Ba to the metallicity, i.e.,  $[\text{Ba}/\text{Fe}] = 0$ .
- La (Lanthanum,  $Z = 57$ ) — We investigated one La II line, 11874.19 Å, using the observed spectra. This line is included in both VALD and MB99 but not in KURZ. Based on the synthetic spectra, the line is expected to be as deep as 0.05 in many objects at  $T_{\text{eff}} \lesssim 6000$  K and reach  $\sim 0.2$  in depth in the two lowest- $T_{\text{eff}}$  objects. However, the depths we measured are consistent with zero for most objects and we could not confirm this line in any of the observed spectra.
- Ce (Cerium,  $Z = 58$ ) — We investigated 22 Ce II lines using the observed spectra. All of these are at  $\lambda < 10000$  Å and listed in VALD, but not included in KURZ or MB99. Most of the lines are expected to be significantly blended with other lines. We detected two lines at 9805.49 Å and 9853.11 Å; they are also blended with other lines, but clearly appear in the shoulders of the contaminating lines. The observed depths of the two lines, where significant, are larger than predicted based on the synthetic spectra by a factor of  $\sim 5$ . There may be a couple of other Ce II lines visible in the observed spectra, although we could not conclude that they are real. In the case of Ce II 9774.63, the spectra of the two objects with the lowest  $T_{\text{eff}}$  show absorption, but their  $\alpha_{\text{obs}}/e$  values, 1.5–1.8, suggest that the detection is marginal. While no significant blend of stellar lines is expected, the telluric absorption may disturb the observed spectra at around this line. The  $\alpha_{\text{obs}}/e$  values for Ce II 9889.47 are significant for a couple of objects with low  $T_{\text{eff}}$ , but strong blending lines, Fe I 9889.035 and CN 9890.1513, prevent us from confirming it. There seems to be an absorption line at the wavelength of Ce II 9949.45 in a few objects, but it looks more significant in stars with intermediate  $T_{\text{eff}}$ , 5000–6500 K. Such  $T_{\text{eff}}$  dependency is inconsistent with the  $T_{\text{eff}}$  trend of the Ce II line predicted with the synthetic spectra.
- Sm (Samarium,  $Z = 62$ ) — We investigated four Sm II lines using the observed spectra. They are listed in VALD, but KURZ includes none. One of them is at  $\lambda > 10000$  Å but not listed in MB99. We found that all the four lines may be present but it is not easy to make firm conclusions. The predicted depths of these lines are rather small;  $\alpha$  is expected to be smaller than  $\sim 0.03$  in our objects except the two with the lowest  $T_{\text{eff}}$ ,  $\sim 4100$  K. In the low- $T_{\text{eff}}$  objects, however, larger depths are predicted to be accompanied by severe blends, and we could not confirm any Sm II line significantly. In contrast, we made significant and marginal detections of some lines in warmer objects. For Sm II 9850.67 and 9936.51 (included in Table 2), the significant absorption was found in two objects for the former and in three objects for the latter in addition to marginal detections in a few more objects. The  $\alpha_{\text{obs}}/e$  for Sm II 10083.34 was  $\sim 2.5$  for the coolest objects, HD 52005, and marginal, 1–2, in a few objects. However, this line is significantly blended with Cr I 10083.18, and the  $T_{\text{eff}}$  trend of the  $\alpha_{\text{obs}}$  is similar to that of the contaminating line. We could not confirm the presence of this Sm II line. We also found that  $\alpha_{\text{obs}}/e$



for Sm II 9788.96 is not zero for some objects; larger than 2 for HD 20902 and 1–2 for HD 194093 and HD 204867. In this case, however, the dependency of the absorption on  $T_{\text{eff}}$  and  $\log g$  is inconsistent with the prediction based on the synthetic spectra. In addition, this line is located where the telluric absorption is relatively strong (Sameshima et al. 2018a). In this paper, we conclude that we detected the two lines, Sm II 9850.67 and 9936.51, but further confirmation and characterization based on spectra of higher resolution and/or higher quality are desired for all the four candidate lines.

- Eu (Europium,  $Z = 63$ ) — We investigated five Eu II lines using the observed spectra. The one at 10019.52 Å is listed in MB99. We detected this line in addition to two new lines at 9898.30 and 10165.56 Å. For all of them, the detection is clearest in HD 194093, which is enhanced in rare-earth elements as mentioned in Section 2.1. We also found that the three lines are significant or at least marginally significant in HD 204867, while they were marginally detected in a few more objects. For Eu II 10019.52,  $\alpha_{\text{obs}}/e$  are approximately 8 and 4 for HD 194093 and HD 204867, respectively. The  $\log gf$  in MB99 seems to predict the observed depths slightly better than the values in KURZ and VALD. The synthetic spectra predict that Fe I 11019.79 and Si I 10020.07 similarly contaminate the Eu II line for the two objects. While the Fe I line is included in both VALD and MB99 and its EP and  $\log gf$  are consistent in the two lists, the Si I line is not included in MB99. The latter is much weaker than suggested with the VALD list even if it exists, and this explains the inconsistency between the observed and synthetic spectra presented in Figure 3 (see the panel for Eu II 10019.52 available as the online material). For the other two lines detected, 9898.30 and 10165.56 Å, there are telluric lines that may disturb the detection of the Eu II lines. We examined the spectra before and after the telluric correction together with the telluric spectra and also the target spectra of individual exposures, and they suggest that the Eu II lines are real. The other two lines at 10034.22 and 10142.99 Å were not detected.
- Dy (Dysprosium,  $Z = 66$ ) — We investigated four Dy II lines, listed in VALD only, using the observed spectra. None of them are found in MB99 although three are located at  $\lambda > 10000$  Å. The KURZ list does not include those lines either. We clearly detected the line at 10523.39 Å in several objects although the overall fits between the observed and synthetic spectra tend to be poor in the surrounding wavelength range. For this line, the  $\log gf$  in VALD predicts reasonable depths that are comparable with the measured. We found clear absorption at the wavelength of Dy II 10305.36 in many objects. The absorption line looks reasonably isolated except the objects with the lowest  $T_{\text{eff}}$ . However, the measured depths are significantly larger than predicted by  $\sim 0.8$  dex in the logarithm of depth. Moreover, the temperature dependency of the depths does not follow the prediction well. In fact, the trend of  $\alpha_{\text{obs}}^*$  is similar to some of the unidentified lines, discussed in Section B, that get stronger towards the lower temperature, while Dy II should get strongest at around 5000 K. Although this Dy II line may exist, there seems to be an unidentified line, at almost the same wavelength, which makes it hard to confirm the Dy II line. We cannot include this line in the list of confirmed lines. The other two lines, Dy II 9763.05 and 10835.94, were not detected.
- Er (Erbium,  $Z = 68$ ) — We investigated one Er II line using the observed spectra. This line at 11059.56 Å is not listed in KURZ or MB99. According to the prediction based on the synthetic spectra, the line is shallow across the temperature range we investigated. The depth may be as deep as  $\sim 0.03$  only in stars with  $T_{\text{eff}} \sim 5000$  K and  $\log g \lesssim 0.5$ , but such objects were not included in this study and we could not detect this line in any object.

## B. DETECTION OF UNIDENTIFIED LINES

Some lines are clearly significant in the observed spectra but not found in the synthetic spectra. Table 3 lists such unidentified lines whose depths are sufficiently large,  $\sim 0.05$  or more, at least in a few objects and show systematic trends with  $T_{\text{eff}}$ . Spectra of five objects, regardless of the significance in each object, around the wavelengths of the unidentified lines are presented in Figure 5 with which one can trace the  $T_{\text{eff}}$  trend of each line between 4000 and 7200 K. The KURZ list was used for the synthetic spectra in Figure 5, but none of the KURZ, VALD, and MB lists has the unidentified lines. Many of the lines get deeper towards the lower (or higher) end of the  $T_{\text{eff}}$  range we investigated, but some lines show a peak within the temperature range of our targets or a rather flat trend (e.g., 9994.9 and 12571.1 Å).

**Table 3.** Absorption lines not predicted by the synthetic spectra

$\lambda_{\text{air}}$ (Å)	Comments
$Y$ band	
9994.9	Blended at $T_{\text{eff}} \lesssim 5000$ K by a couple of CN lines (the strongest is at 9995.10 Å), but there is an unknown line which gets strongest at around 5500 K.
10071.8	Stronger towards the lower temperature.
10133.5	Stronger towards the lower temperature. Maybe this is the Fe I line listed in both KURZ and VALD at a different wavelength, 10134.21 Å, that has no counterpart in the observed spectra (see text).
10163.6	Synthetic spectra have almost no absorption at around 4500–5000 K, but a clear line was detected. Fe II 10163.606 may be present in some objects, but it is expected to be significant only at $> 5000$ K.
10185.5	Stronger towards the lower temperature.
10243.7	Stronger towards the lower temperature.
10271.2	Stronger towards the lower temperature.
10273.1	Stronger towards the lower temperature. There are two lines, CN 10272.93 Å and Ca I 10273.68 Å, blending with this unknown line, but they cannot explain the absorption detected.
10277.3	Stronger towards the lower temperature.
10305.3	Stronger towards the lower temperature.
10338.5	Stronger towards the lower temperature.
10387.1	Stronger towards the lower temperature.
10427.3	Stronger towards the lower temperature.
10434.0	There are a couple of contaminating CN lines dominant at $\gtrsim 5000$ K, but this unknown line is stronger towards the higher temperature. It is probably C I 10433.35 listed in KURZ (but not in VALD) which is not seen in the observed spectra at the given wavelength.
10476.5	Synthetic spectra have almost no absorption at $T_{\text{eff}} \gtrsim 4500$ K, but there is a clear line whose depth seems to show a peak at $\sim 5000$ K. This line may be a CN line (see text).
10512.8	Stronger towards the lower temperature.
10542.5	Synthetic spectra have almost no absorption at $T_{\text{eff}} \gtrsim 4500$ K, but there is a clear line whose depth seems to show a peak at 4500–5000 K.
10549.5	Blended with N I 10549.64 at $T_{\text{eff}} \gtrsim 6000$ K and with Cr I 10550.095 at $T_{\text{eff}} \lesssim 4500$ K, but there is clearly a line, unexpected in the synthetic spectra, whose depth seems to show a peak at the intermediate $T_{\text{eff}}$ range.
10587.1	Strongest at around 4500–5000 K.
10625.4	Stronger towards the lower temperature. Synthetic spectra have almost no absorption at this wavelength at the entire $T_{\text{eff}}$ range. The observed absorption resembles Fe I 10622.592 in the synthetic spectra although the latter is not confirmed in the observed spectra.
10657.4	Stronger towards the lower temperature.
10696.5	Observed spectra seem to show two lines not visible in the synthetic spectra. One of them gets stronger towards the lower temperature, while the other is seen at around 6000 K.
11050.3	Stronger towards the lower temperature and seen at only $T_{\text{eff}} \lesssim 5000$ K.
11083.7	Stronger towards the lower temperature and seen at only $T_{\text{eff}} \lesssim 5000$ K.
$J$ band	
11742.0	Stronger towards the lower temperature and seen at only $T_{\text{eff}} < 5000$ K.
11784.9	Stronger towards the lower temperature.
11833.0	Stronger towards the lower temperature.
11910.6	Stronger towards the lower temperature and seen at only $T_{\text{eff}} \lesssim 5000$ K. At the higher $T_{\text{eff}}$ , in contrast, a weak line of C I is visible at 11910.62 Å.
11923.2	Stronger towards the lower temperature.

*Table 3 continued*

**Table 3** (*continued*)

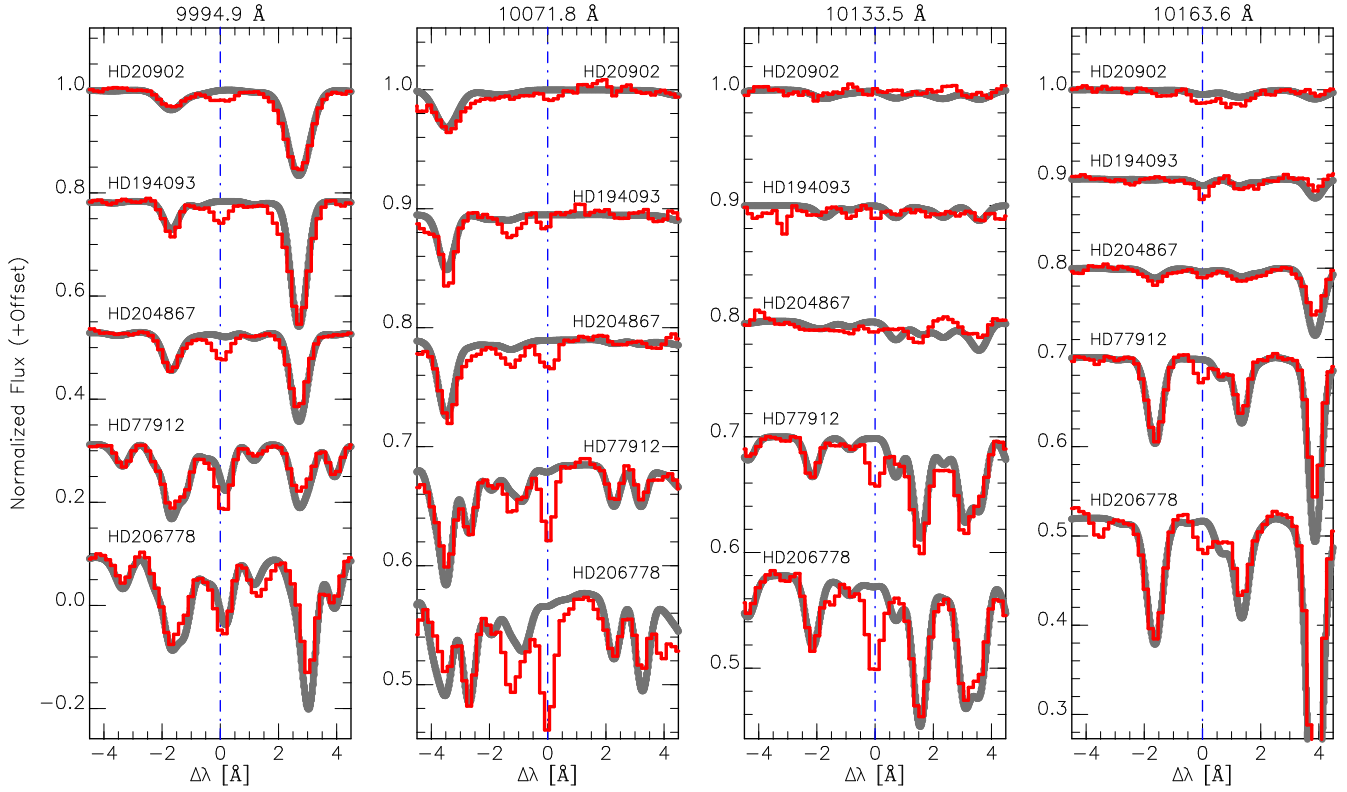
$\lambda_{\text{air}}$ (Å)	Comments
12097.5	Stronger towards the lower temperature and seen at only $T_{\text{eff}} \lesssim 5000$ K. At the higher $T_{\text{eff}}$ , in contrast, a weak line of C I is visible at 12097.49 Å.
12290.7	Blended with CN 12291.332, but clearly present in a wide range of $T_{\text{eff}}$ and stronger towards the lower temperature.
12351.8	Strongest at around the intermediate temperatures, $\sim 5000$ K.
12357.9	Stronger towards the lower temperature.
12457.0	Seems to be stronger towards the lower temperature, but the $T_{\text{eff}}$ dependency is weak.
12476.9	Strongest at around 5000 K.
12499.8	Blended with a couple of CN lines at $T_{\text{eff}} \lesssim 5000$ K, but there is a line showing a different trend with a peak at $\sim 5000$ K.
12571.1	The $T_{\text{eff}}$ trend seems flat for a wide $T_{\text{eff}}$ range, 4000–5500 K.
12635.0	Strongest at around the intermediate temperatures, $\sim 5000$ K.
12658.9	The $T_{\text{eff}}$ trend seems consistent with that of the combination of two lines of Ni I at 12655.38 and 12655.60 Å listed in both KURZ and VALD (see text).
12737.8	Blended with Ti I 12738.383 together with other weaker lines, but there is a clear line, at the shoulder of the Ti I line, which is unexpected in the synthetic spectra.
12884.8	Stronger towards the lower temperature.
12916.3	Stronger towards the lower temperature.
13016.4	Stronger towards the lower temperature.
13088.8	There are strong telluric absorption lines around this wavelength, but there is a reasonably strong line which shows a well-behaved trend with the temperature, getting stronger towards the lower temperature.

Table 3 does not include lines which appear both in the observed and synthetic spectra consistently even if the predicted depths are significantly shallower than those in the observed. For example, the observed spectra show a clear line at 10516.1 Å which is almost invisible in the spectra synthesized with KURZ or VALD. This line is probably Ca I 10516.14 (EP=4.74 eV,  $\log gf = -0.52$  dex) as listed in MB99. VALD and KURZ also list this line but give a significantly smaller  $\log gf$  value,  $-1.438$  dex. If we use the  $\log gf$  in MB99 for the spectral synthesis, the line observed is explained reasonably well. Therefore, we do not include this line in Table 3. In fact, inconsistency in line strengths between the observed and synthetic spectra is found in many lines, e.g., Mg I 12456.935 and a pair of N I 12461.25 and CN 12460.83 that give different contribution according to  $T_{\text{eff}}$ , showing much stronger absorption in the observed; they are outside the scope of this paper and not included in Table 3.

As long as one of the three lists (KURZ, VALD, and MB99) gives good identification of the observed feature, Table 3 does not include such a line even if the other two lists cannot explain the feature. For example, we found that Fe I 10452.75 (EP=3.88 eV) is listed

in MB99 but not in KURZ and VALD. While warmer stars ( $T_{\text{eff}} \gtrsim 5000$  K) show a C I line listed in all the line lists almost at the same wavelength, the absorption in low- $T_{\text{eff}}$  stars requires the Fe I line in MB99. Moreover, this line was included in the abundance measurements by Kondo et al. (2019) and gave [Fe/H] values within 0.03 dex of the final results based on dozens of Fe I lines. In the case of S I 10635.97 listed in MB99, in contrast, KURZ and VALD list this line with the wavelength of 10633.08 Å. The observed spectra show the absorption at around the wavelength given in MB99. The EP and  $\log gf$  of this line are consistent in all the three lists, and the predicted depths as a function of  $T_{\text{eff}}$  agree with those observed.

For some of the unidentified lines in Table 3, different lines at almost the same wavelength were confirmed in both observed and synthetic ones at a particular  $T_{\text{eff}}$  range but the observed spectra show unexpected absorption with a completely different trend against the temperature, which indicates the presence of the unidentified lines. At around 10434.0 Å, for example, a CN line is seen at lower temperatures,  $T_{\text{eff}} \lesssim 5500$  K, and this line appears in both the observed and synthetic spectra. However, we found another line, which is the unidentified line we report, growing with increasing  $T_{\text{eff}}$ .



**Figure 5.** Absorption lines that were not predicted in the synthetic spectra (Table 3). The red and gray curves indicate the observed and synthetic spectra, respectively. The wavelength of each line is indicated by the vertical line and labeled at the top of each panel. The spectra of five stars with different  $T_{\text{eff}}$  (increasing from top to bottom) are presented, even if the given line is not seen in each star, to show its dependence on  $T_{\text{eff}}$ . The complete figure set (45 panels) is available in the online journal.

Some lines in Table 3 seem to have counterparts in some line lists but at different wavelengths (and no list gives the observed wavelength). In the following, we give remarks on such lines that seem to give the corresponding absorption, in the observed spectra, at shifted wavelengths and show the consistent  $T_{\text{eff}}$  trends as predicted.

10133.5 Å — The Fe I line listed in KURZ and VALD with the wavelength of 10134.21 Å roughly follows the  $T_{\text{eff}}$  trend of the absorption at 10133.5 Å in the observed spectra. The observed spectra do not show the absorption at 10134.21 Å. The predicted  $T_{\text{eff}}$  trend of the Fe I line is slightly different by itself from the observed at the lowest temperatures around 4000 K, but this deviation may be explained by the blend with Ti I 10133.39 and

some molecular lines. No line is listed in MB99 around this wavelength.

10476.5 Å — The observed  $T_{\text{eff}}$  trend may be explained by a CN line. There is, in fact, one CN line at 10475.295 Å, listed in KURZ and VALD, which appears rather shallow in the observed spectra even if it exists. Maybe the wavelength in VALD should be replaced by 10476.5 Å or, instead, there is another CN line which gives the observed wavelength and strengths. No line is listed in MB99 around this wavelength.

12658.9 Å — Interestingly, the feature predicted with two Ni I lines at 12655.38 and 12655.60 Å shows the  $T_{\text{eff}}$  trend consistent with the observed, but no significant absorption was observed in our 13 targets at the given wavelengths. The two Ni I lines, present in both KURZ and VALD, seem to give similar contributions to the feature, although MB99 lists only one line at 12655.60 Å.

## REFERENCES

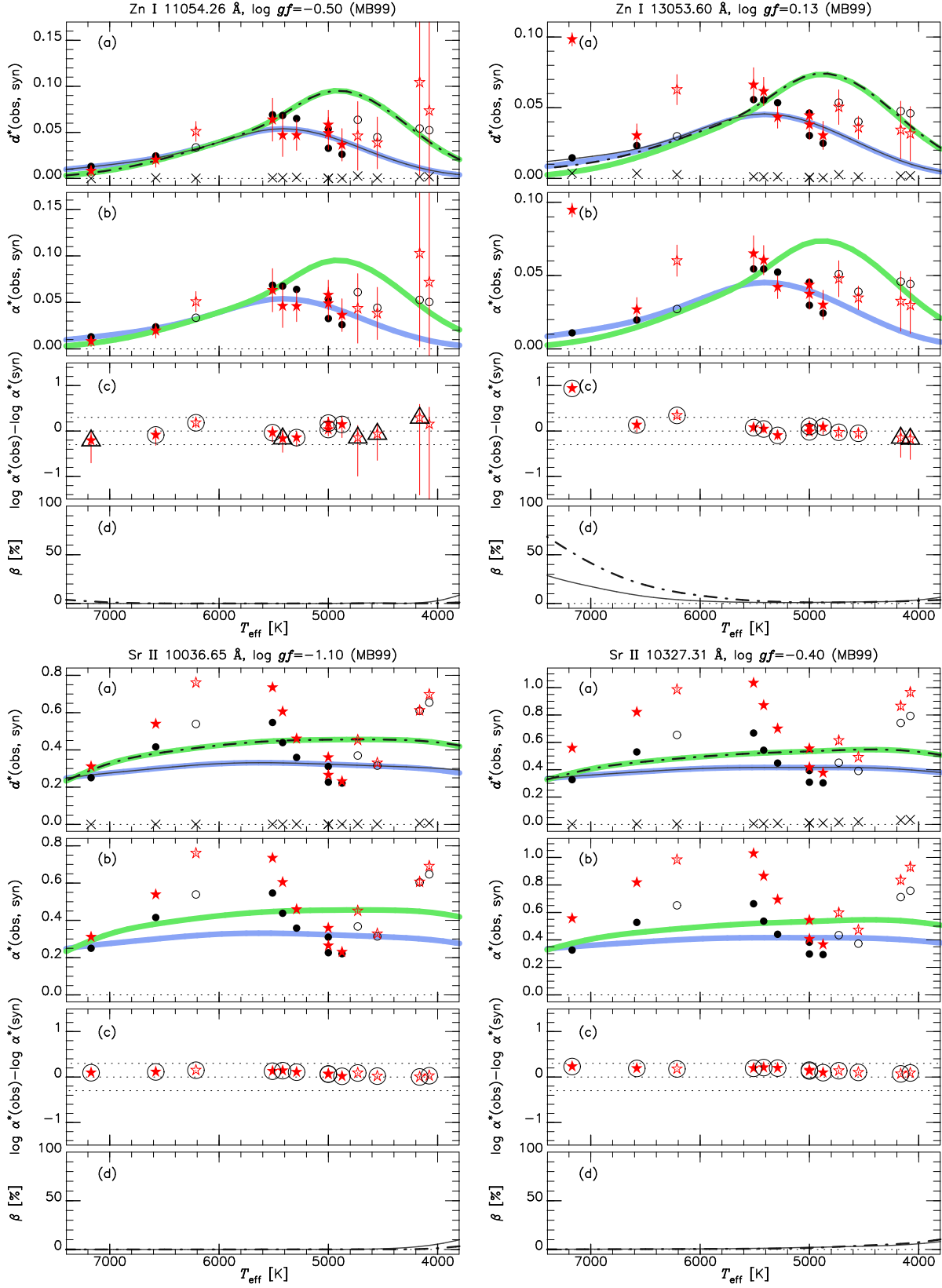
- Abbott, B. P., Abbott, R., Abbott, T. D., et al. 2017, *PhRvL*, 119, 161101
- Adams, W. S., & Joy, A. H. 1926, *PASP*, 38, 322
- Adams, W. S., & Joy, A. H. 1927, *Proceedings of the National Academy of Science*, 13, 393
- Afşar, M., Sneden, C., Wood, M. P., et al. 2018, *ApJ*, 865, 44

- Andreasen, D. T., Sousa, S. G., Delgado Mena, E., et al. 2016, *A&A*, 585, A143
- Andrievsky, S. M., Lépine, J. R. D., Korotin, S. A., et al. 2013, *MNRAS*, 428, 3252
- Andrievsky, S. M., Luck, R. E., & Korotin, S. A. 2014, *MNRAS*, 437, 2106
- Asplund, M., Grevesse, N., Sauval, A. J., & Scott, P. 2009, *ARA&A*, 47, 481
- Battistini, C., & Bensby, T. 2016, *A&A*, 586, A49
- Bensby, T., Feltzing, S., & Oey, M. S., 2014, *A&A*, 562, A71
- Bisterzo, S., Gallino, R., Straniero, O., et al. 2011, *MNRAS*, 418, 284
- Böcek Topcu, G., Afşar, M., Sneden, C., et al. 2019, *MNRAS*, 485, 4625
- Burris, D. L., Pilachowski, C. A., Armandroff, T. E., et al. 2000, *ApJ*, 544, 302
- Burris, D., Lusk, J., & Jones, E. M. 2009, *PASP*, 121, 111
- Busso, M., Gallino, R., & Wasserburg, G. J. 1999, *ARA&A*, 37, 239
- Caffau, E., Andrievsky, S., Korotin, S., et al. 2016, *A&A*, 585, A16
- Chen, X., Wang, S., Deng, L., et al. 2019, *Nature Astronomy*, 3, 320
- Chojnowski, S. D., Hubrig, S., Hasselquist, S., et al. 2019, *ApJL*, 873, L5
- Cunha, K., Smith, V. V., Hasselquist, S., et al. 2017, *ApJ*, 844, 145
- da Silva, R., Lemasle, B., Bono, G., et al. 2016, *A&A*, 586, A125
- Dékány, I., Hajdu, G., Grebel, E. K., & Catelan, M. 2019, *ApJ*, 883, 58
- Delgado Mena, E., Tsantaki, M., Adibekyan, V. Z., et al. 2017, *A&A*, 606, A94
- D’Orazi, V., Magrini, L., Randich, S., et al. 2009, *ApJ*, 693, L31
- Duffau, S., Caffau, E., Sbordone, L., et al. 2017, *A&A*, 604, A128
- Genovali, K., Lemasle, B., Bono, G., et al. 2014, *A&A*, 566, A37
- Gratton, F., Bragaglia, A., Carretta, E., & Tosi, M. 2006, *ApJ*, 642, 462
- Gray, D. F., & Toner, C. G. 1986, *ApJ*, 310, 277
- Gray, R. O., Graham, P. W., & Hoyt, S. R. 2001, *AJ*, 121, 2159
- Hasselquist, S., Shetrone, M., Cunha, K., et al. 2016, *ApJ*, 833, 81
- Hekker, S., & Meléndez, J. 2007, *A&A*, 475, 1003
- Hempel, M., Stancliffe, R. J., Lugaro, M., & Meyer, B. S. 2016, *ApJ*, 831, 171
- Hirai, Y., Saito, T. R., Ishimaru, Y., & Wanajo, S. 2018, *ApJ*, 855, 63
- Hotokezaka, K., Beniamini, P., & Piran, T. 2018, *International Journal of Modern Physics D*, 27, 1842005
- Hubrig, S., Castelli, F., Gonzalez, J. F., et al. 2012, *A&A*, 542, A31
- Ikeda, Y., Kobayashi, N., Kondo, S., et al. 2016, *Proc. SPIE*, 9908, 99085Z
- Ji, A. P., Frebel, A., Chiti, A., et al. 2016, *Nature*, 531, 610
- Ji, A. P., & Frebel, A. 2018, *ApJ*, 856, 138
- Jofré, P., Heiter, U., Worley, C. C., et al. 2017, *A&A*, 601, A38
- Johnson, H. M. 1975, *ApJ*, 200, 395
- Karakas, A. I., & Lattanzio, J. C. 2014, *PASA*, 31, e030
- Kaeufl, H.-U., Ballester, P., Biereichel, P., et al. 2004, *Proc. SPIE*, 1218
- Kondo, S., Fukue, K., Matsunaga, N., et al. 2019, *ApJ*, 875, 129
- Kovtyukh, V. V. 2007, *MNRAS*, 378, 617
- Kovtyukh, V. V., & Andrievsky, S. M. 1999, *A&A*, 351, 597
- Kovtyukh, V. V., Soubiran, C., Belik, S. I., & Gorlova, N. I. 2003, *A&A*, 411, 559
- Kovtyukh, V. V., Soubiran, C., Bienaymé, O., Mishenina, T. V., & Belik, S. I. 2006, *MNRAS*, 371, 879
- Kurucz, R. L., 1993, *Kurucz CD-ROM 13, ATLAS 9 Stellar Atmosphere Programs and 2 km/s Grid* (Cambridge: SAO)
- Lemasle, B., François, P., Genovali, K., et al. 2013, *A&A*, 558, A31
- Lundqvist, M., Wahlgren, G. M., & Hill, V. 2007, *A&A*, 463, 693
- Luck, R. E., & Lambert, D. L. 1985, *ApJ*, 298, 782
- Luck, R. E. 2014, *AJ*, 147, 137
- Luck, R. E. 2018, *AJ*, 156, 171
- Luck, R. E., & Lambert, D. L. 2011, *AJ*, 142, 136
- Luck, R. E., Andrievsky, S. M., Kovtyukh, V. V., et al. 2011, *AJ*, 142, 51
- Lyubimkov, L. S., Lambert, D. L., Korotin, S. A., et al. 2015, *MNRAS*, 446, 3447
- Majewski, S. R., Schiavon, R. P., Frinchaboy, P. M., et al. 2017, *AJ*, 154, 94
- Matsunaga, N., Bono, G., Chen, X., et al. 2018, *SSRv*, 214, 74
- McWilliam, A. 1997, *ARA&A*, 35, 503
- McWilliam, A., Wallerstein, G., & Mottini, M. 2013, *ApJ*, 778, 149
- Meléndez, J., & Barbuy, B. 1999, *ApJS*, 124, 527
- Oliva, E., Origlia, L., Maiolino, R., et al. 2012, *Proc. SPIE*, 8446, 84463T

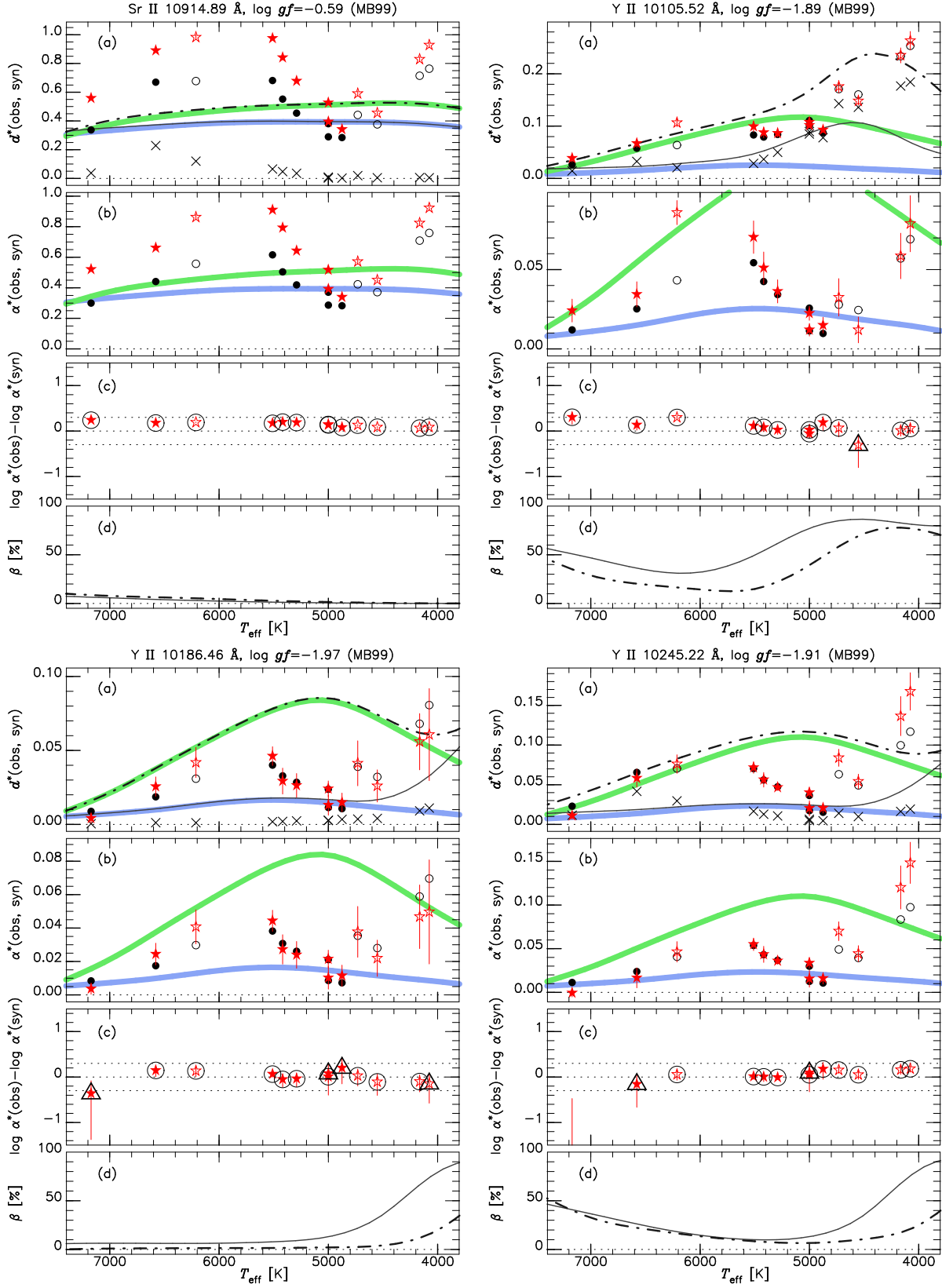


- Önehag, A., Heiter, U., Gustafsson, B., et al. 2012, *A&A*, 542, A33
- Origlia, L., Oliva, E., Maiolino, R., et al. 2013, *A&A*, 560, A46
- Origlia, L., Oliva, E., Sanna, N., et al. 2016, *A&A*, 585, A14
- Otsubo, S., Ikeda, Y., Kobayashi, N., et al. 2016, *Proc. SPIE*, 9908, 990879
- Park, C., Jaffe, D. T., Yuk, I.-S., et al. 2014, *Proc. SPIE*, 9147, 91471D
- Roach, F. E. 1942, *ApJ*, 96, 272
- Ryabchikova, T., Piskunov, N., Kurucz, R. L., et al. 2015, *PhyS*, 90, 054005
- Ryabchikova, T., Piskunov, N., Pakhomov, Y., et al. 2016, *MNRAS*, 456, 1221
- Sameshima, H., Matsunaga, N., Kobayashi, N., et al. 2018a, *PASP*, 130, 74502
- Sameshima, H., Ikeda, Y., Matsunaga, N., et al. 2018b, *ApJS*, 239, 19
- Schultz, R. H., & Armentrout, P. B. 1991, *JChPh*, 94, 2262
- Sellwood, J. A., Binney, J. J. 2002, *MNRAS*, 336, 785
- Siegel, D. M., Barnes, J., & Metzger, B. D. 2019, *Nature*, 569, 241
- Skowron, D. M., Skowron, J., Mróz, P., et al. 2019, *Science*, 365, 478
- Smartt, S. J., Chen, T.-W., Jerkstrand, A., et al. 2017, *Nature*, 551, 75
- Smith, V. V., Cunha, K., Shetrone, M. D., et al. 2013, *ApJ*, 765, 16
- Snedden, C., Gratton, R.G., & Crocker, D. A. 1991, *A&A*, 246, 354
- Snedden, C., Cowan, J. J., & Gallino, R. 2008, *ARA&A*, 46, 241
- Snedden, C., Bean, J., Ivans, I., et al. 2012, MOOG: LTE line analysis and spectrum synthesis, *Astrophysics Source Code Library* (ascl:1202.009)
- Steel, H. M. 1945, *ApJ*, 102, 43
- Takeda, Y., Kang, D.-I., Han, I., et al. 2013, *MNRAS*, 432, 769
- Tanaka, M., Utsumi, Y., Mazzali, P. A., et al. 2017, *PASJ*, 69, 102
- Taniguchi, D., Matsunaga, N., Kobayashi, N., et al. 2018, *MNRAS*, 473, 4993
- Tody, D. 1986, *Proc. SPIE*, 733
- Tody, D. 1993, *Astronomical Data Analysis Software and Systems II*, 173
- Tsujimoto, T., & Nishimura, N. 2018, *ApJL*, 863, L27
- Tsujimoto, T., & Baba, J. 2019, *ApJ*, 878, 125
- Udalski, A., Soszyński, I., Pietrukowicz, P., et al. 2018, *AcA*, 68, 315
- Wallace, L., Livingston, W., Hinkle, K., & Bernath, P. 1996, *ApJS*, 106, 165
- Zhang, J., Cui, W., & Zhang, B. 2010, *MNRAS*, 402, 956

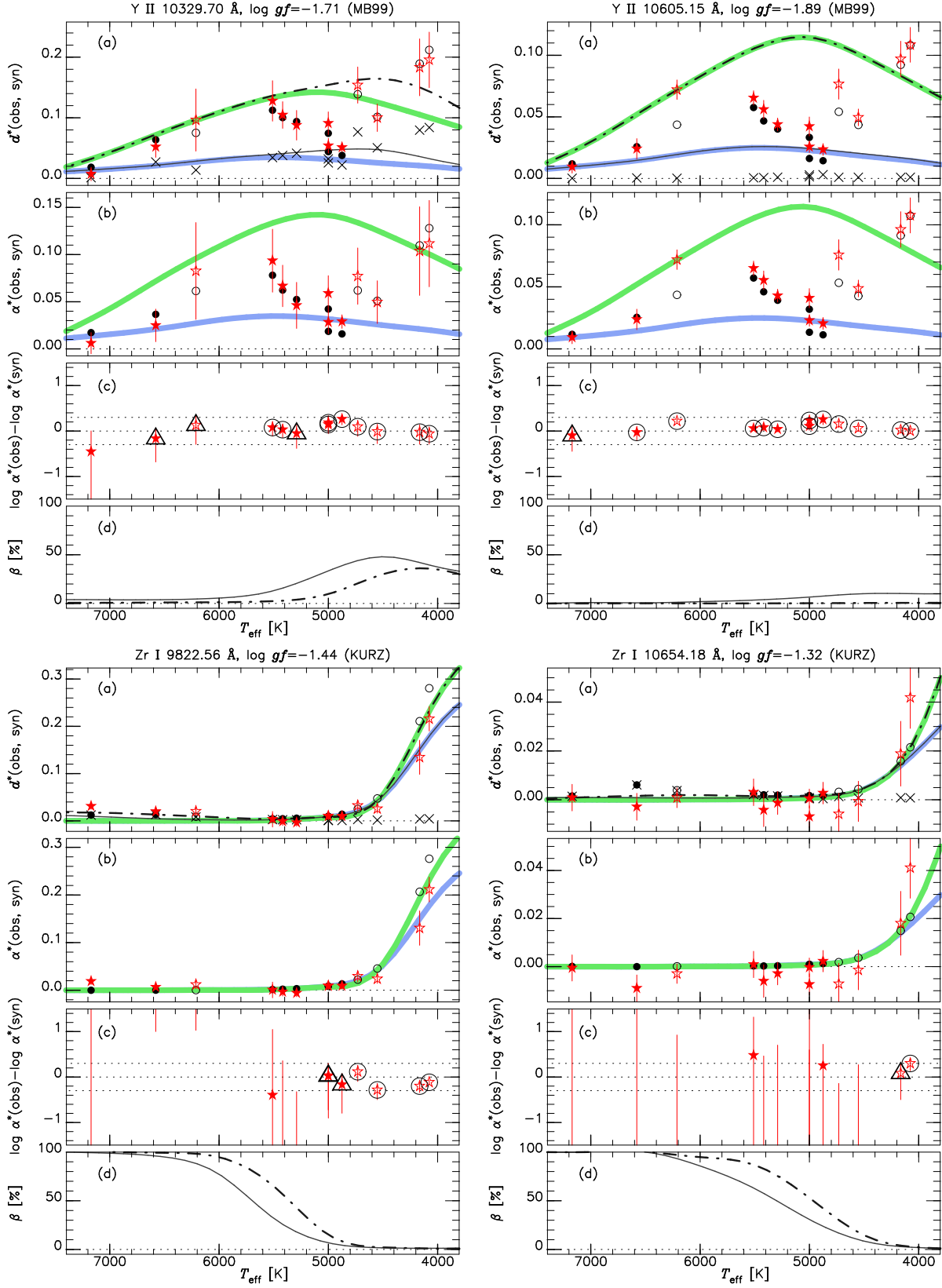
Here presented are individual plots for Figure 2 which are available as the online material.



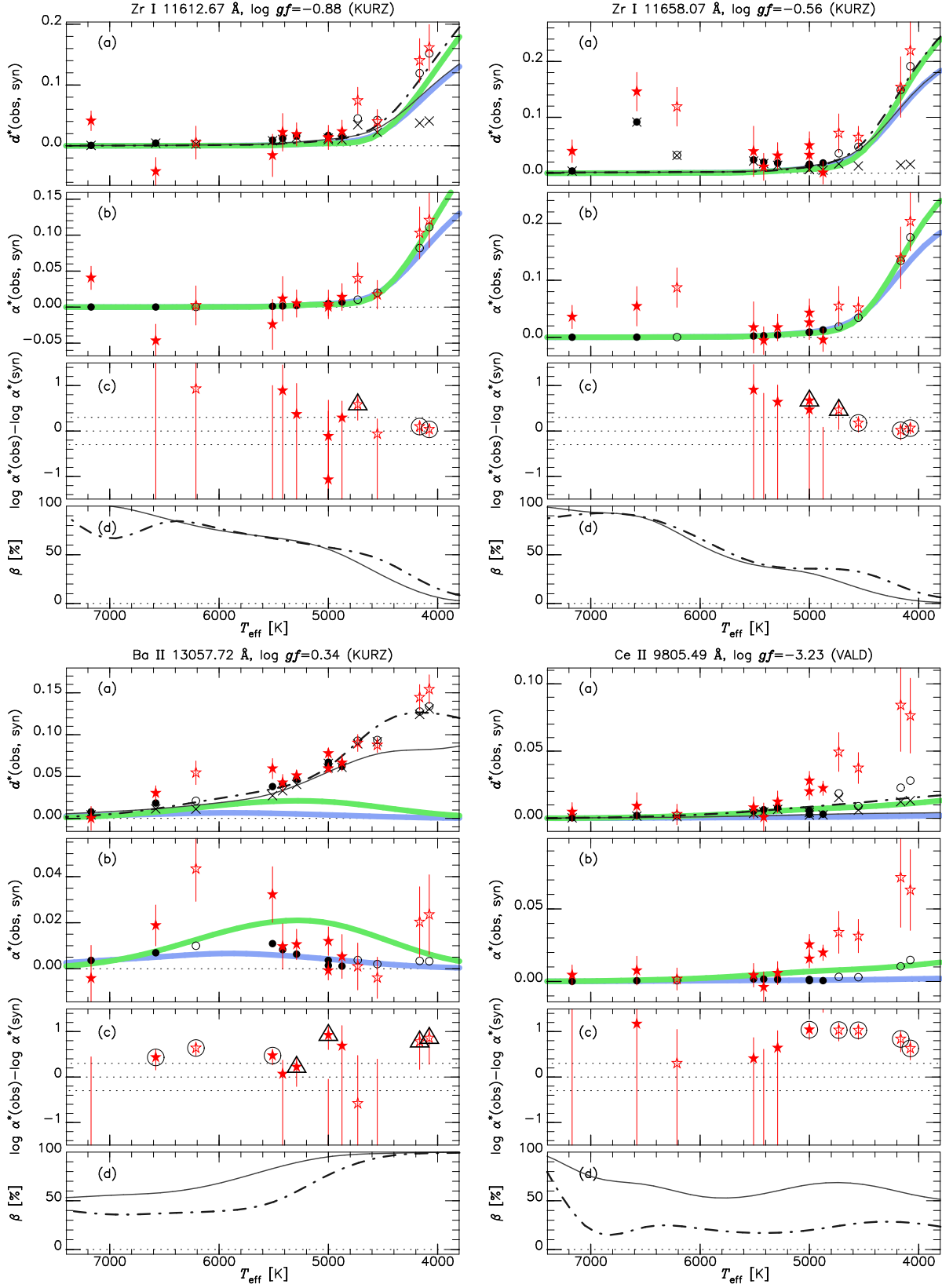
Here presented are individual plots for Figure 2 which are available as the online material.



Here presented are individual plots for Figure 2 which are available as the online material.

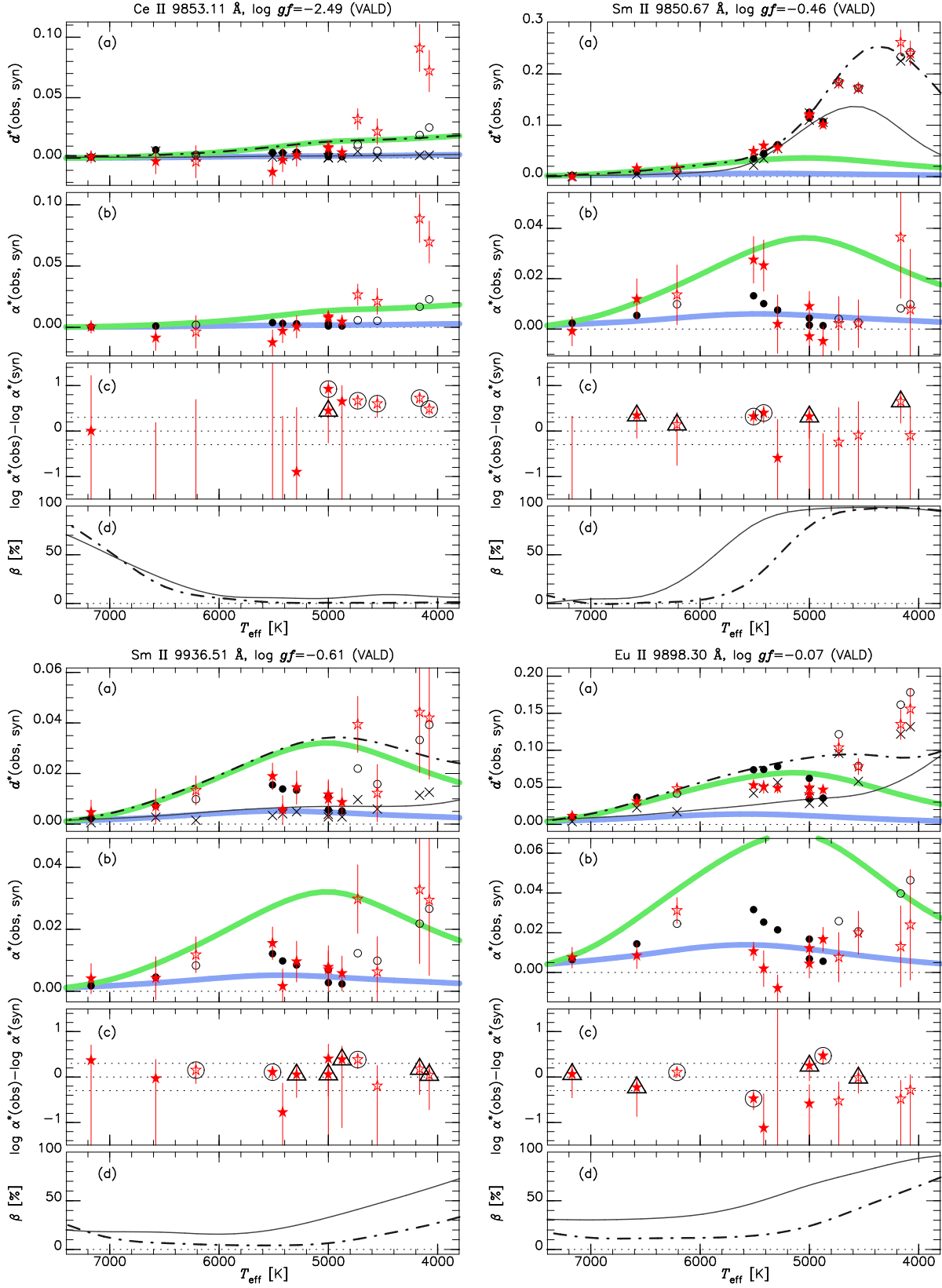


Here presented are individual plots for Figure 2 which are available as the online material.

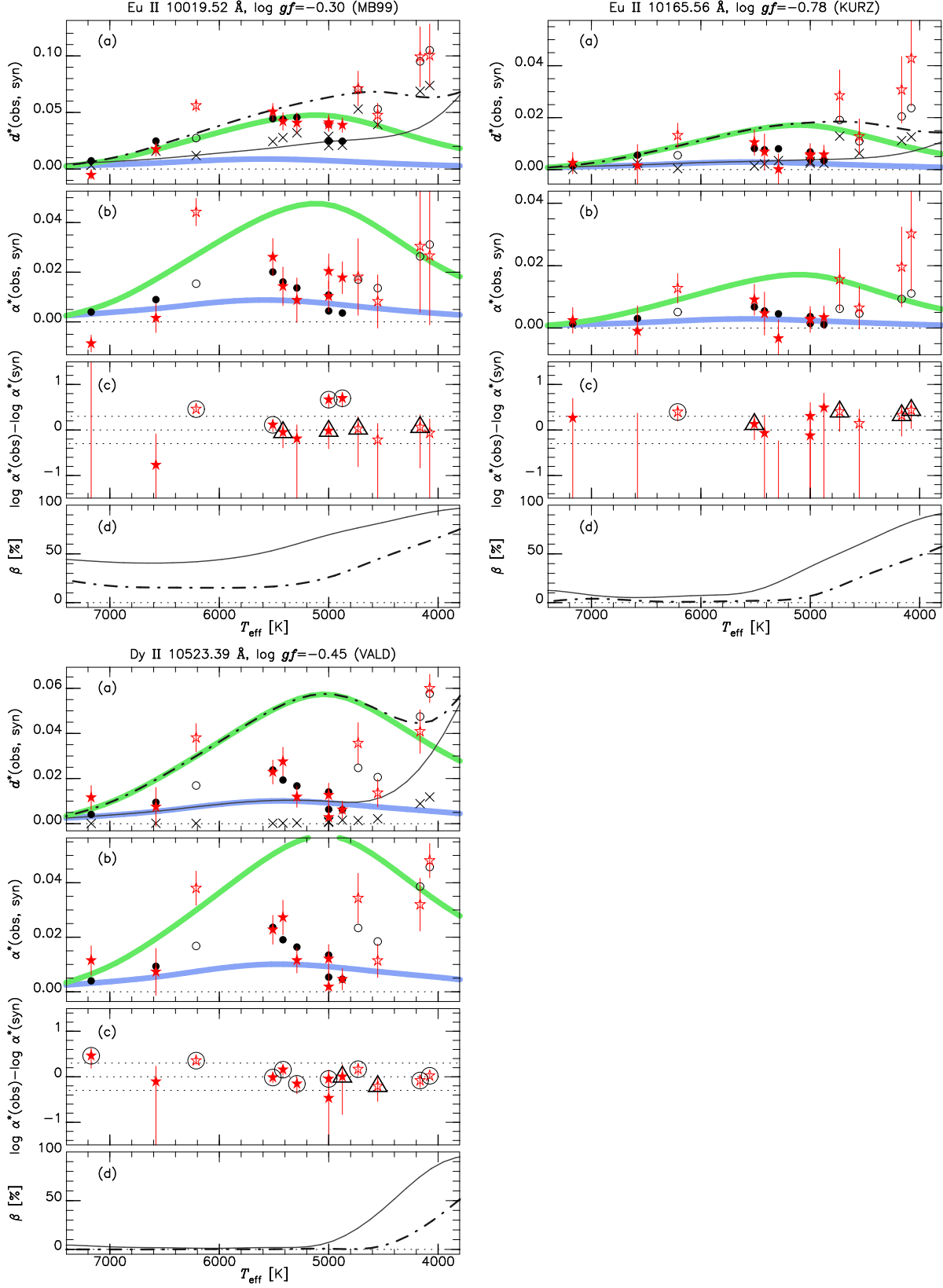




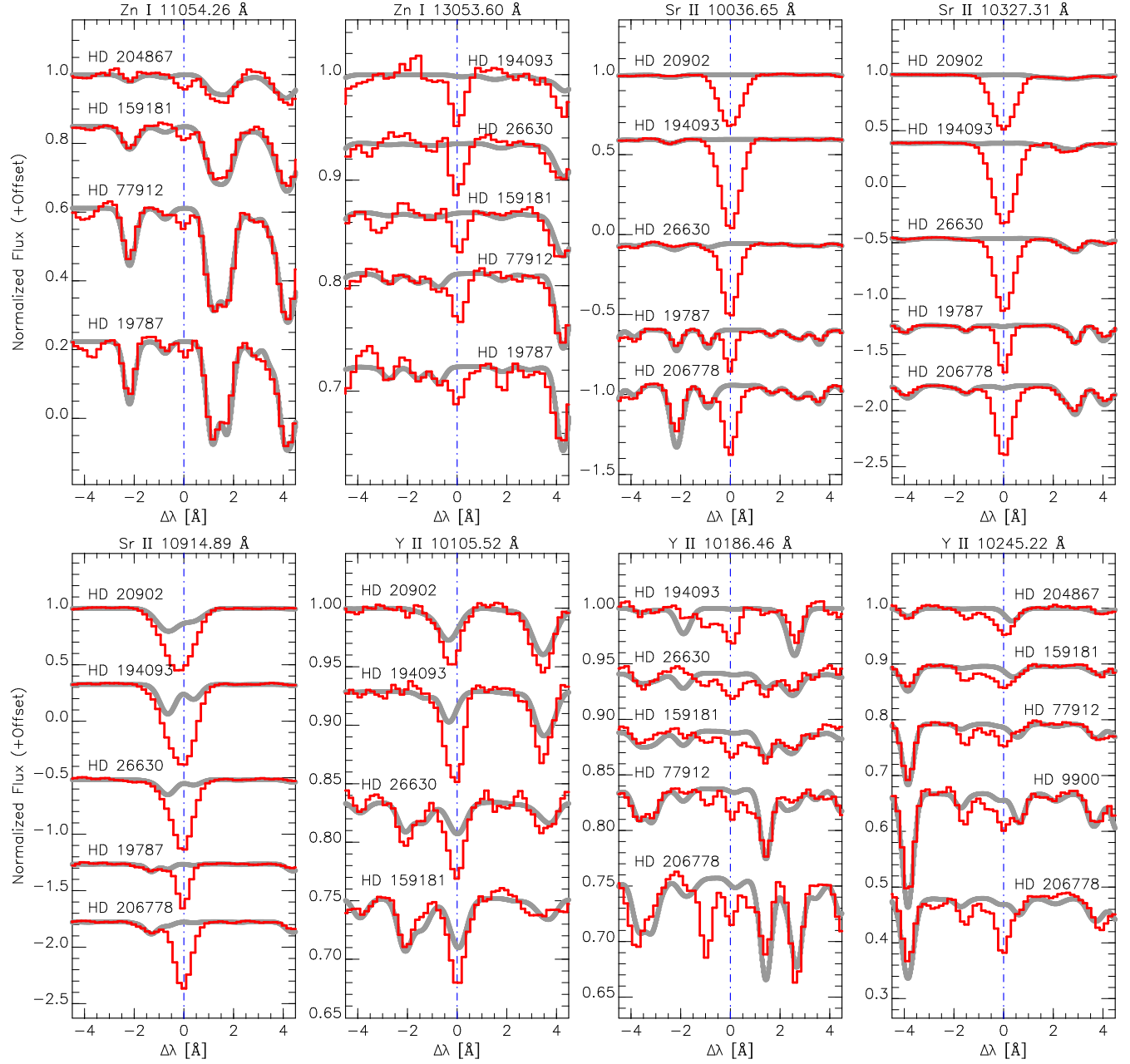
Here presented are individual plots for Figure 2 which are available as the online material.



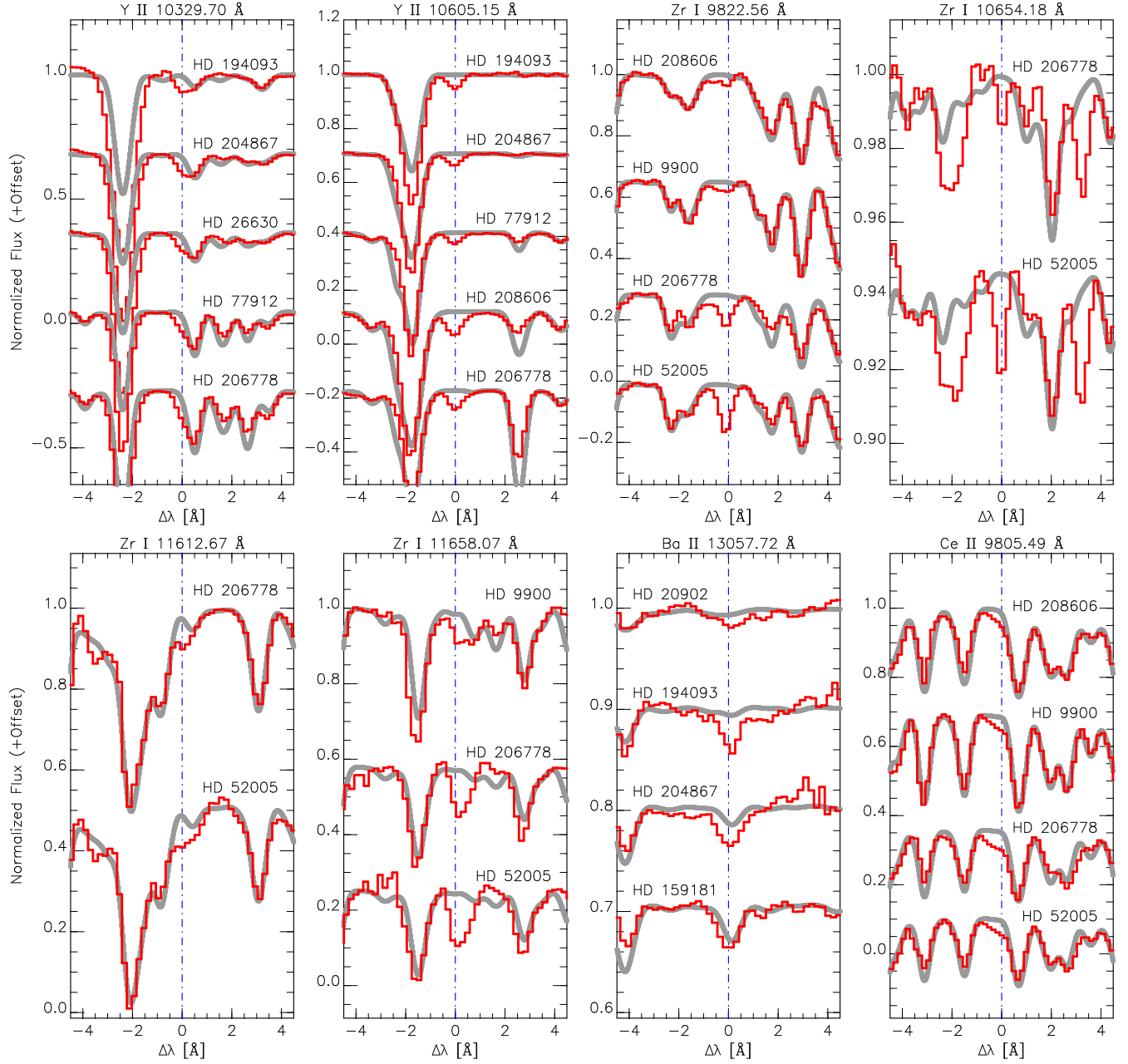
Here presented are individual plots for Figure 2 which are available as the online material.



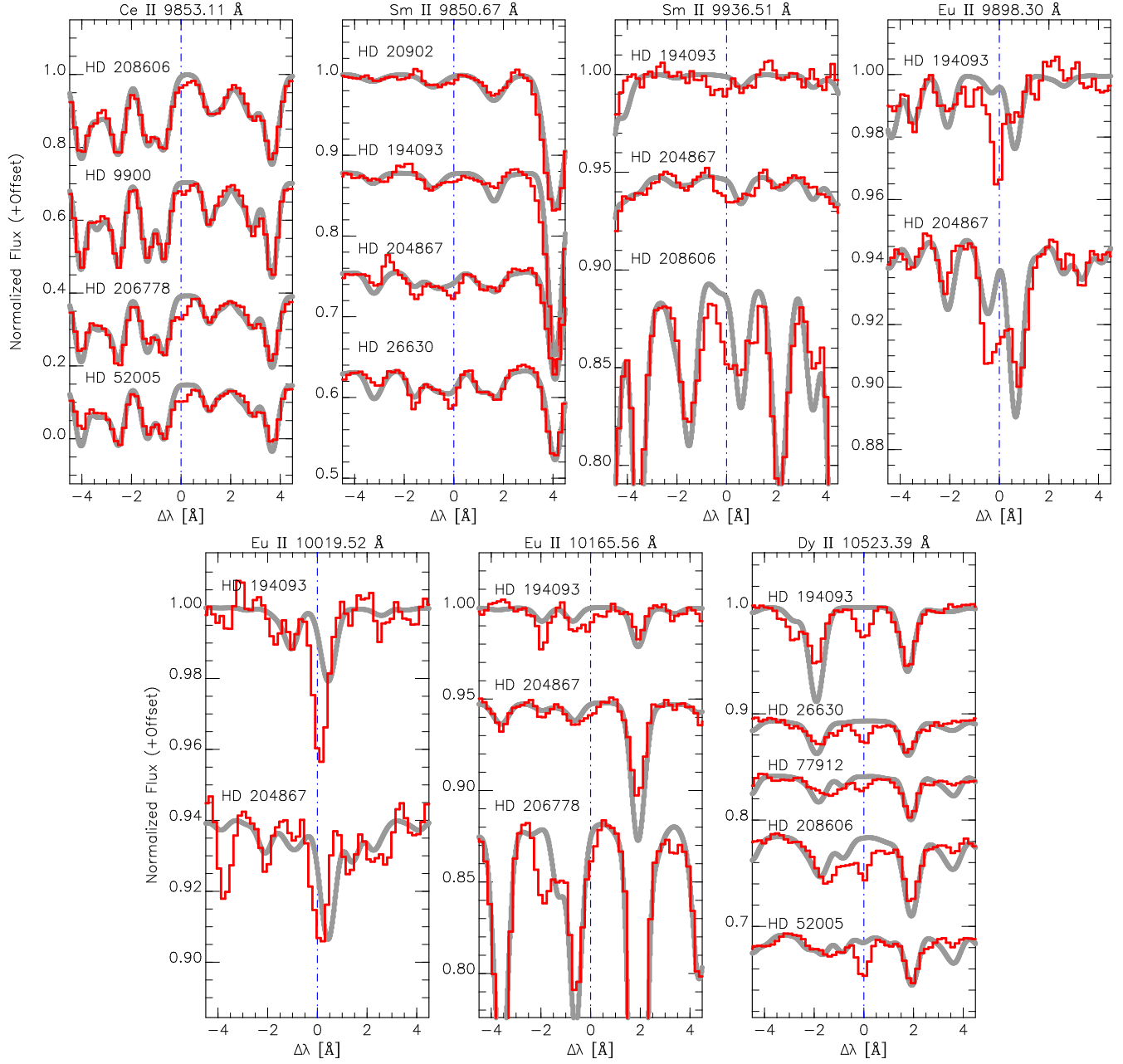
Here presented are individual plots for Figure 3 which are available as the online material.



Here presented are individual plots for Figure 3 which are available as the online material.

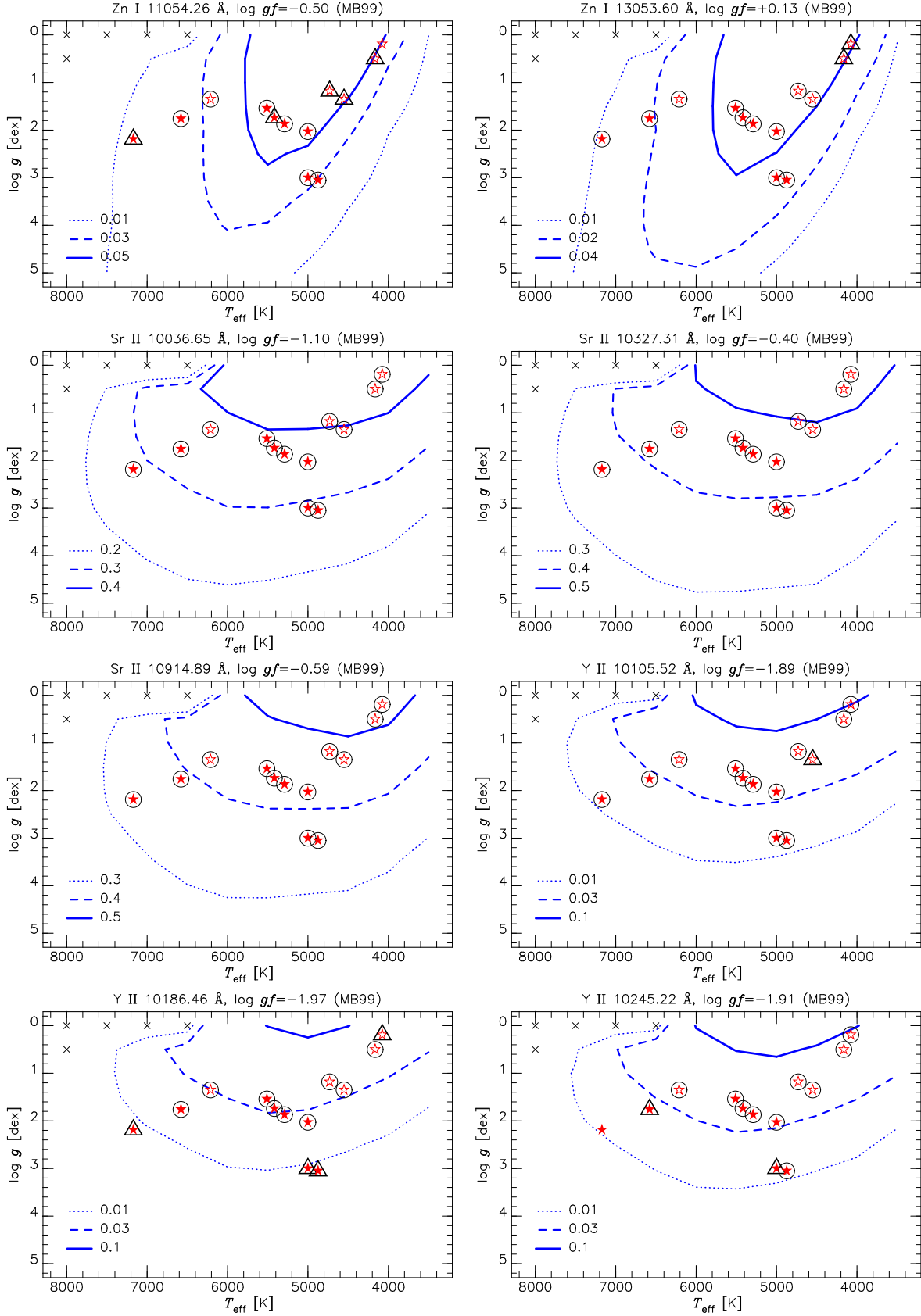


Here presented are individual plots for Figure 3 which are available as the online material.

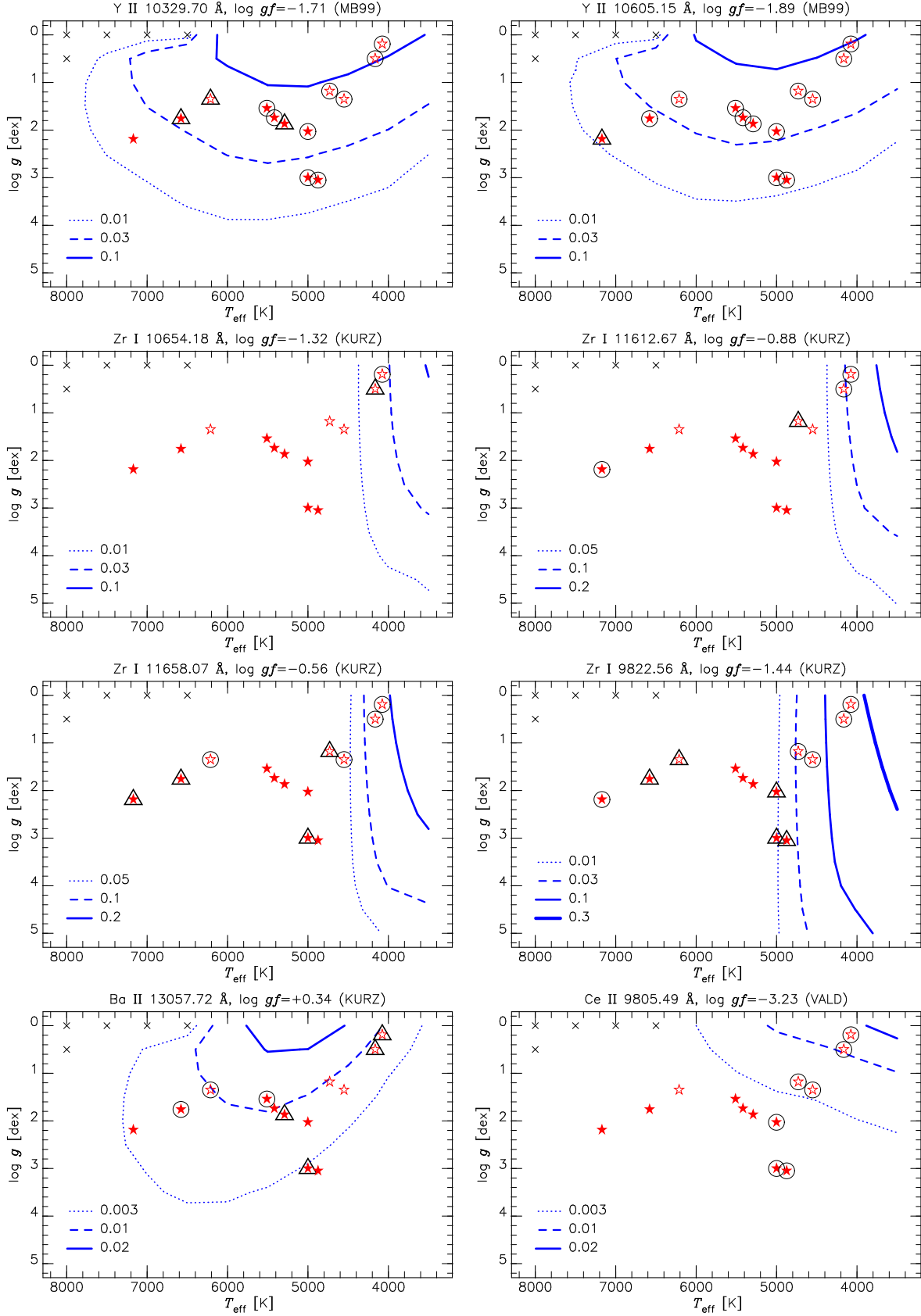




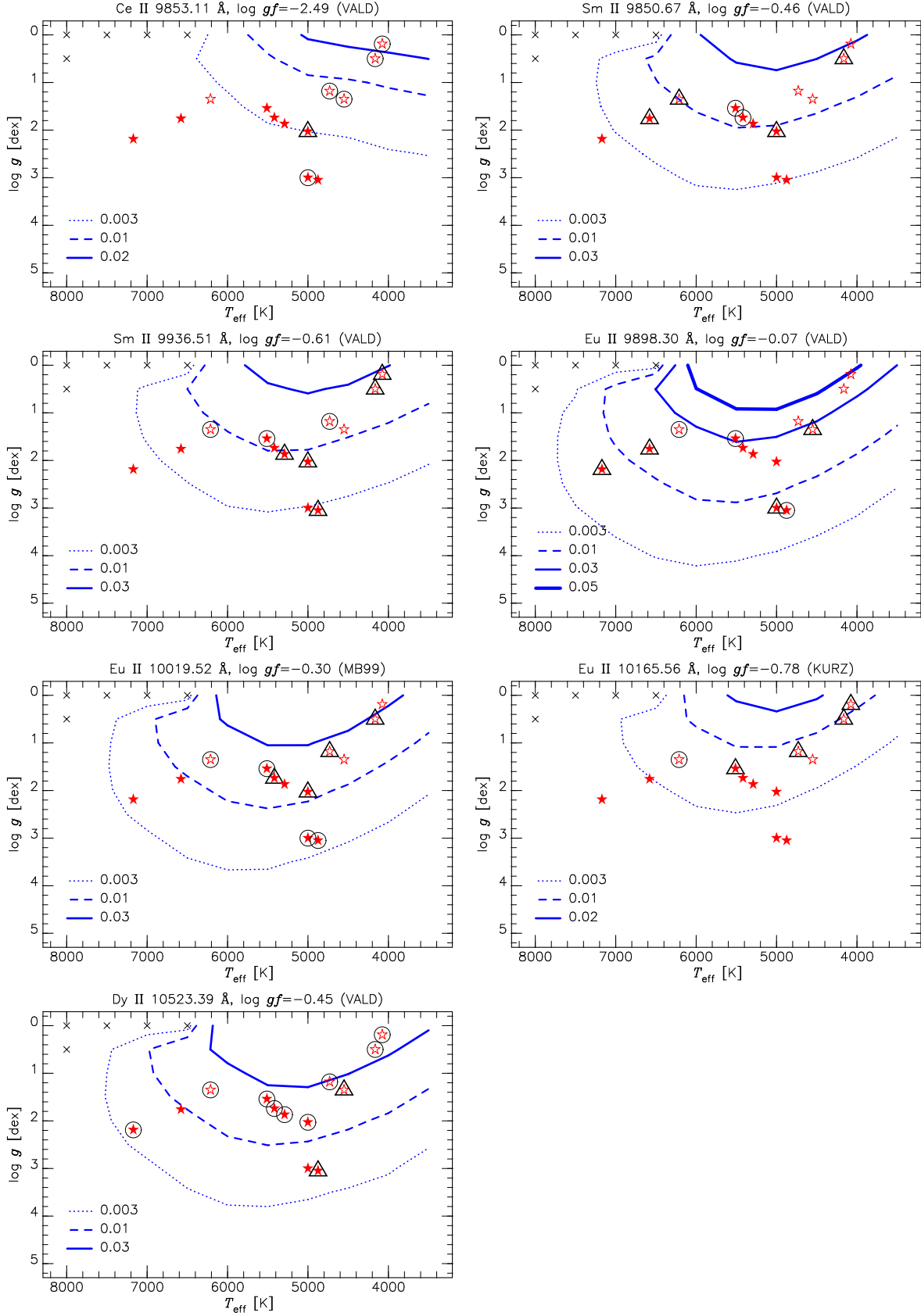
Here presented are individual plots for Figure 4 which are available as the online material.



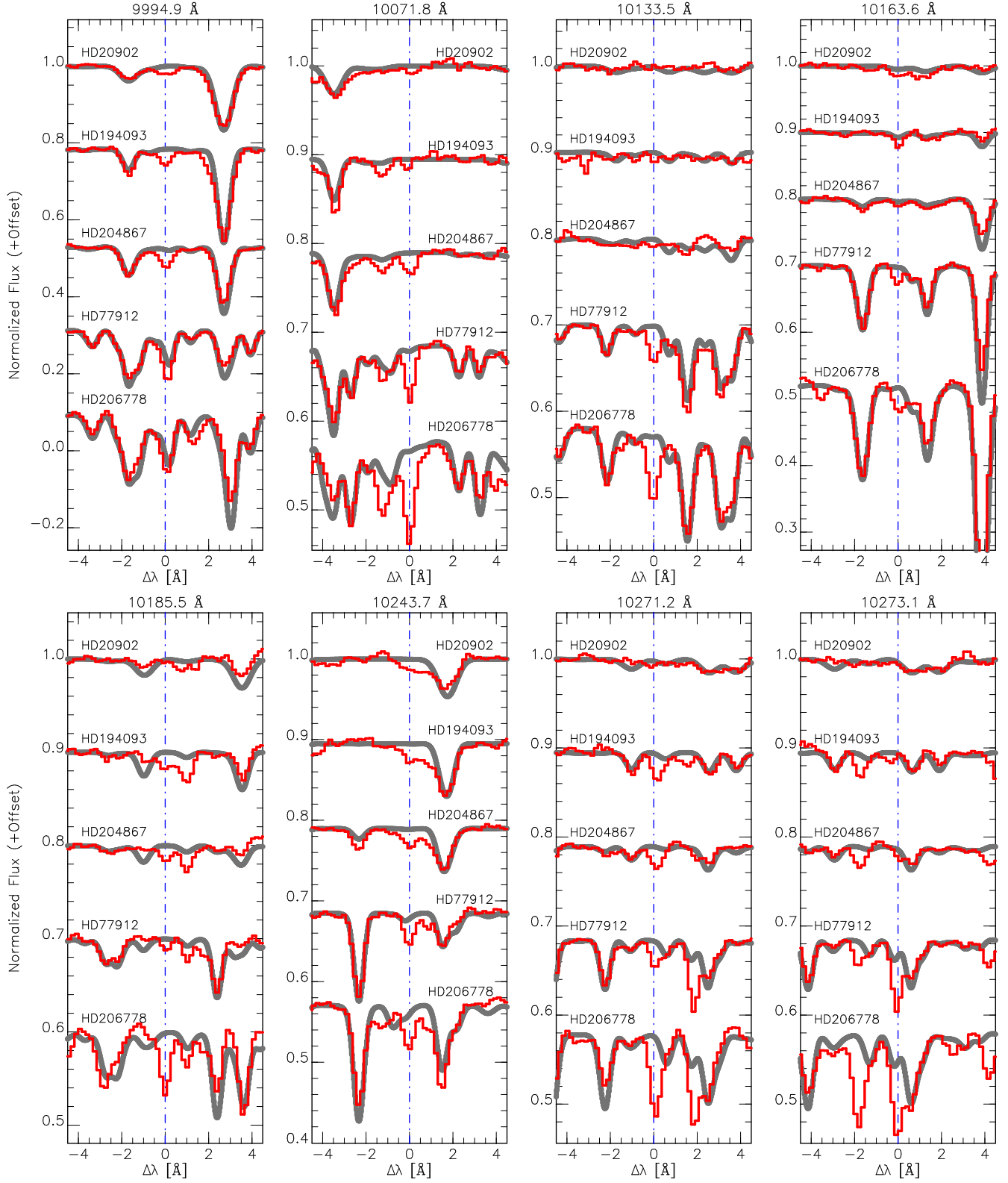
Here presented are individual plots for Figure 4 which are available as the online material.



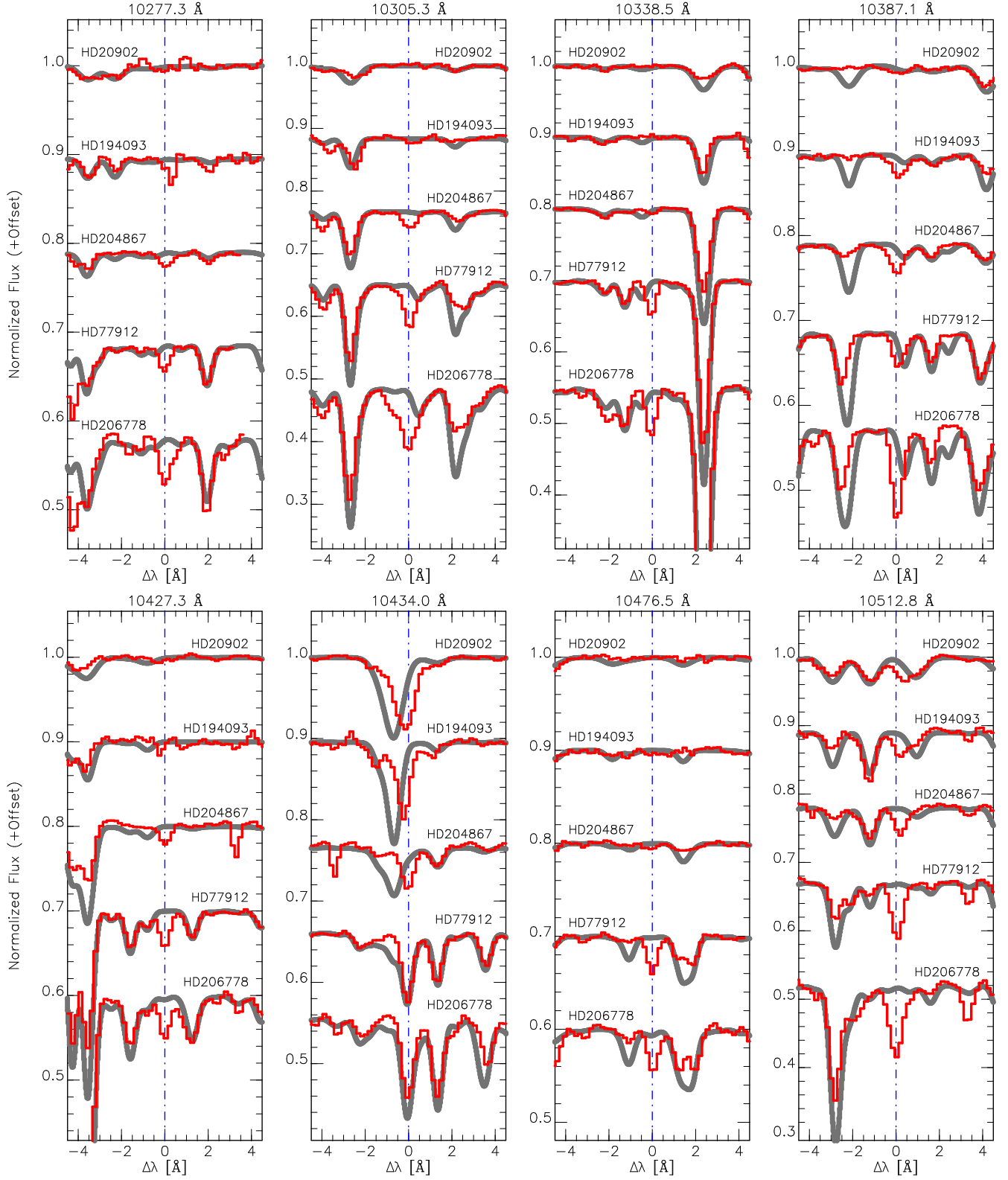
Here presented are individual plots for Figure 4 which are available as the online material.



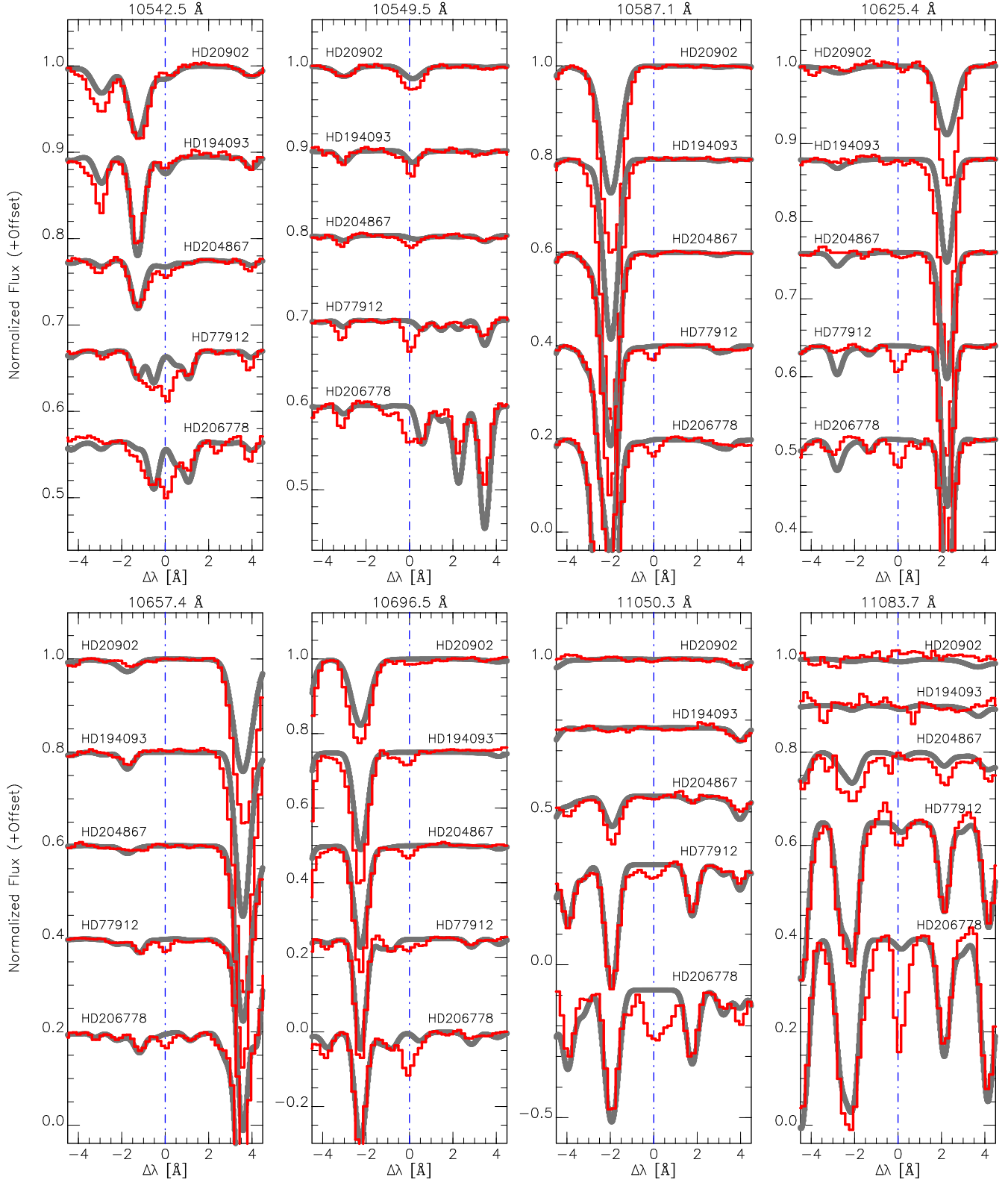
Here presented are individual plots for Figure 5 which are available as the online material.



Here presented are individual plots for Figure 5 which are available as the online material.

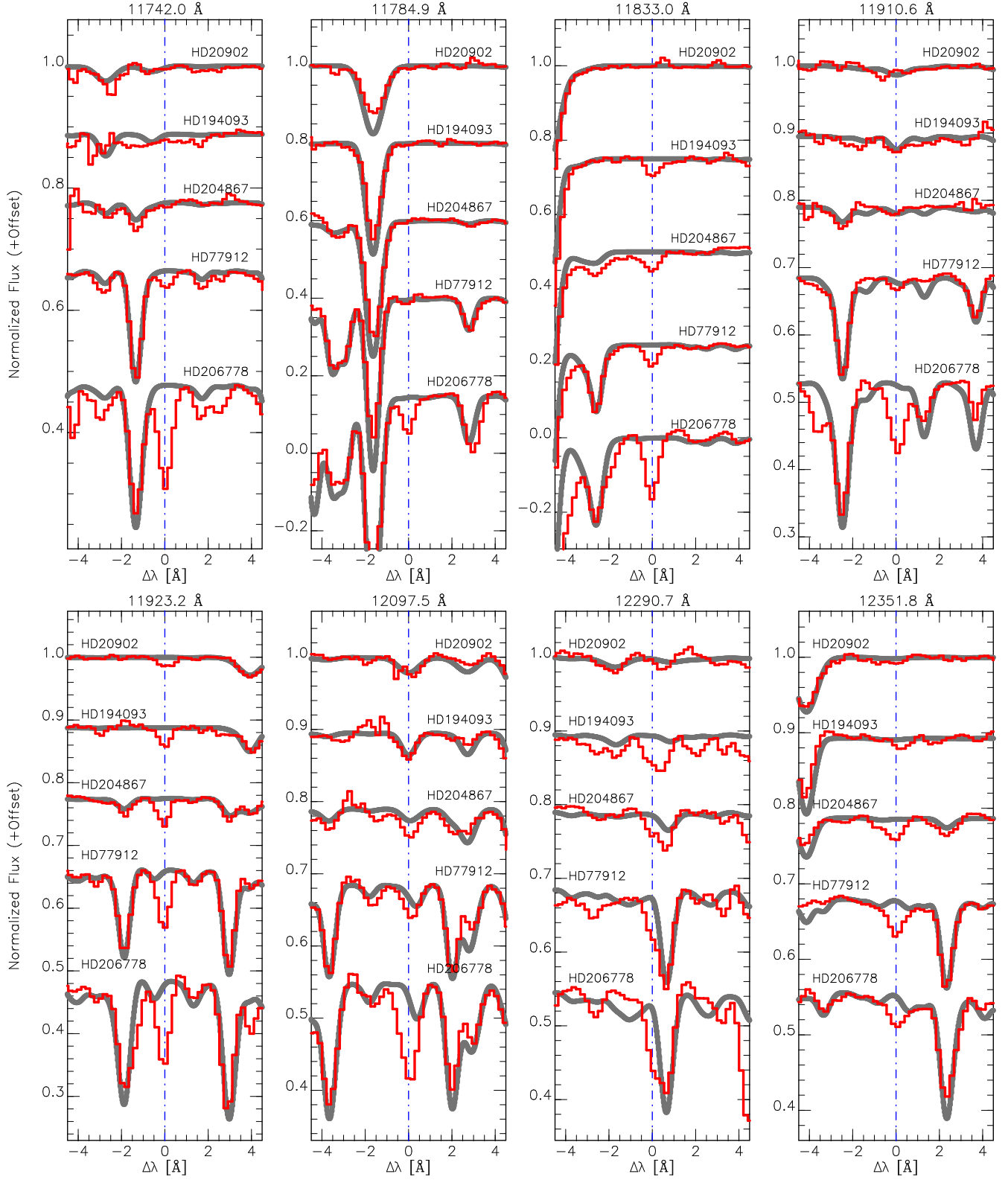


Here presented are individual plots for Figure 5 which are available as the online material.

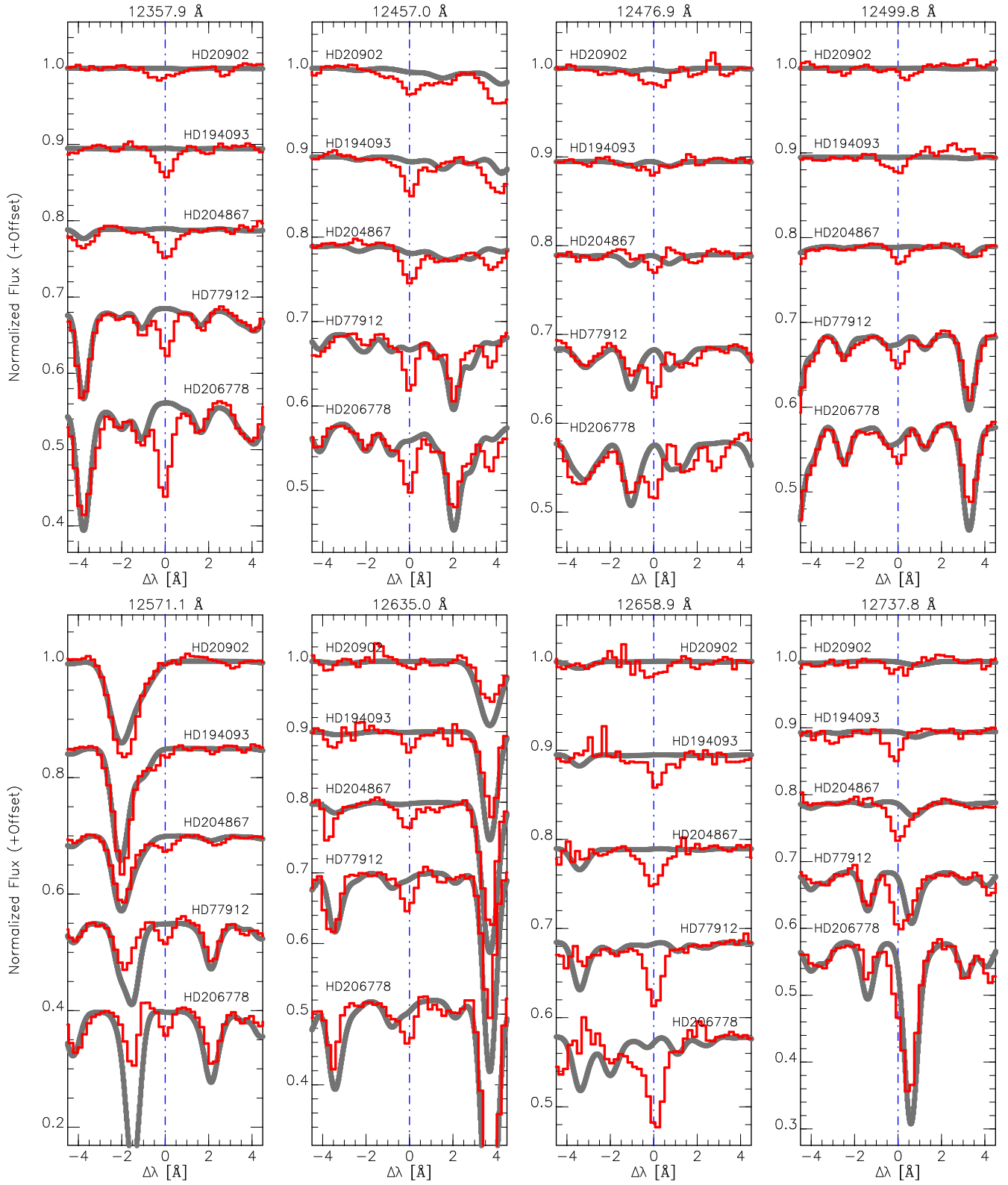




Here presented are individual plots for Figure 5 which are available as the online material.



Here presented are individual plots for Figure 5 which are available as the online material.



Here presented are individual plots for Figure 5 which are available as the online material.

